



HAL
open science

Petrogenesis of late-Variscan high-K alkali-calcic granitoids and calc-alkalic lamprophyres: The Aber-Ildut/North-Ouessant complex, Armorican massif, France

Martial Caroff, Cyrill Labry, Bernard Le Gall, Christine Authemayou, Denise
Bussien Grosjean, Marcel Guillong

► To cite this version:

Martial Caroff, Cyrill Labry, Bernard Le Gall, Christine Authemayou, Denise Bussien Grosjean, et al.. Petrogenesis of late-Variscan high-K alkali-calcic granitoids and calc-alkalic lamprophyres: The Aber-Ildut/North-Ouessant complex, Armorican massif, France. *Lithos*, 2015, 238, pp.140-155. 10.1016/j.lithos.2015.09.025 . insu-01222528

HAL Id: insu-01222528

<https://insu.hal.science/insu-01222528>

Submitted on 30 Oct 2015

HAL is a multi-disciplinary open access archive for the deposit and dissemination of scientific research documents, whether they are published or not. The documents may come from teaching and research institutions in France or abroad, or from public or private research centers.

L'archive ouverte pluridisciplinaire **HAL**, est destinée au dépôt et à la diffusion de documents scientifiques de niveau recherche, publiés ou non, émanant des établissements d'enseignement et de recherche français ou étrangers, des laboratoires publics ou privés.

1 Petrogenesis of late-Variscan high-K alkali-calcic granitoids and calc-
2 alkalic lamprophyres: the Aber-Ildut/North-Ouessant complex,
3 Armorican massif, France

4
5
6 Martial Caroff ^{a,*}, Cyrill Labry ^a, Bernard Le Gall ^a, Christine Authemayou ^a, Denise
7 Bussien Grosjean ^{a,1}, Marcel Guillong ^b

8
9 ^a UMR/CNRS n°6538 « Domaines Océaniques », Institut Universitaire Européen de la Mer,
10 Université de Brest, Place Nicolas Copernic, 29280 Plouzané, France

11 ^b Institute of Geochemistry and Petrology, Department of Earth Sciences, ETH Zurich,
12 Clausiusstrasse 25, 8092 Zurich, Switzerland

13
14
15 * Corresponding author: caroff@univ-brest.fr

16
17
18 ¹ Present address : Musée cantonal de Géologie, Quartier UNIL-Dorigny, Bâtiment
19 Anthropole, 1015 Lausanne, Switzerland.

20

21 Keywords: Leucogranite; Calc-alkaline lamprophyre; Minette; Tetrad effect; Variscan belt;
22 Armorican Massif

23

24 *Abstract*

25 The Aber-Ildut/North-Ouessant Variscan granitoid complex in the Armorican Massif is an
26 example of high-K alkali-calcic zoned pluton, c. 304 Ma in age. A first magmatic batch
27 intruded through a northern EW-trending sinistral transcurrent shear zone, before injecting
28 southwards as a huge horizontal zoned sill, with moderately peraluminous muscovite-free
29 granitoids in the north and strongly peraluminous muscovite-bearing leucogranites to the
30 south. The second magmatic stage resulted in the intrusion of a large two-mica leucogranitic
31 body from a root zone along the same shear zone, prior to the end of crystallization of the first
32 injection. Finally, ultrapotassic dykes, including calc-alkalic lamprophyres (leucominettes),
33 intrude the complex. The strongly peraluminous granites are interpreted as pure melting
34 products of crustal clay-rich pelitic material. All the other petrographic types, including
35 leucominettes, are thought to result from mixing of crustal melts and mantle-derived mafic
36 liquids. Highly silicic tourmaline-bearing leucogranites are significantly affected by a tetrad
37 effect, in relation with REE complexing behavior. Aber-Ildut/North-Ouessant granitoids
38 probably formed during the Variscan late-orogenic stage associated with exhumation and
39 lithospheric thinning, at low pressure and by advective heating of a ≤ 50 km-thick crust from
40 hot metasomatized asthenosphere.

41

42 **1. Introduction**

43

44 High-K alkali-calcic – and calc-alkalic – granitoids are distinctive in their high
45 potassium content and their lack of iron enrichment (Frost et al., 2001). Although many of

46 them are metaluminous, the most siliceous terms are peraluminous (aluminium saturation
47 index > 1). Peraluminous granitoids are mainly divided into S-type granites (Chappell and
48 White, 1974) and muscovite-leucogranites (Barbarin, 1999), two types clearly distinguished
49 on the basis of major elements by Patiño Douce (1999). Following this author, muscovite-
50 leucogranites are pure crustal melt, which is not the case for the S-type granitoids. Sylvester
51 (1998) proposed a supplemental category, with the individualization of strongly peraluminous
52 (SP) granites, when the aluminium saturation index is higher than 1.1.

53 Strongly peraluminous (SP) granites occur generally as isolated plutons within
54 overthickened crust in high pressure collision chains (Alps, Himalaya), and in association
55 with high-K calc-alkalic/alkali-calcic granitoids within ≤ 50 km-thick crust in high
56 temperature chains (Variscides, Lachlan). Both granitoid types are commonly referred to as
57 late- or post-orogenic magmatism (Maniar and Piccoli, 1989; Sylvester, 1998; Barbarin, 1999;
58 Frost et al., 2001).

59 The Aber-Ildut/North-Ouessant granitoid complex (hereafter referred to as AI-NO)
60 belongs to a set of Variscan high-K plutons, c. 300 Ma in age, all located along the northern
61 coast of the Armorican massif (Chauris, 1994). Although divided into three submassifs, the
62 complex constitutes a coherent structure, rooted in a sinistral NE/SW-trending shear zone.
63 The three most remarkable features are: (1) the presence of a large spectrum of petrologic
64 varieties, ranging from quartz monzodiorites to tourmaline leucogranites and leucominettes;
65 (2) the fact that each unit sets up prior to the end of crystallization of that emplaced just
66 before: except for two petrographic types (late microgranitic and microsyenitic dykes), there
67 is on the field either a progressive transition from one unit to another or mingling relations
68 between them; and (3) the coexistence in a single pluton of high-K alkali-calcic moderately
69 peraluminous (MP) granitoids with contemporaneous both strongly peraluminous (SP)
70 leucogranites and calc-alkalic lamprophyres.

71 In this paper, a new set of geochronological, petrologic and geochemical data is
72 presented to discuss the conditions of unit emplacements, the petrogenetic connection
73 between the various granitic/lamprophyric magmas and, lastly, a source model with respect to
74 the late orogenic Armorican context.

75

76 **2. Analytical techniques**

77

78 *2.1. U/Pb zircon dating*

79

80 Zircon grains were extracted by standard mineral separation and placed in epoxy resin.
81 In order to avoid perturbed zones and inherited cores, the grains were polished to their
82 equatorial plane, and then imaged by cathodoluminescence (CL; CamScan MV2300, Earth
83 Sciences Institute, University of Lausanne, Switzerland).

84 Dating was performed by laser ablation (LA) inductively coupled plasma mass
85 spectrometry (ICP-MS) at the Institute of Geochemistry and Petrology (ETH, Zurich,
86 Switzerland), combining a Resonetics Resolution 155 excimer laser (ArF, 193 nm) to a
87 Thermo Element XR magnetic sector mass spectrometer. Laser beam diameter of 30 microns
88 and fluence of c. 2 J/cm² at a frequency of 5 Hz were used. After surface cleaning and wash
89 out, the reading composed of c. 10 seconds of gas blank and 40 seconds of ablation signal
90 started. Ablated material was carried by He flux (0.6 - 0.7 l/min) and sample gas (0.8 - 1.1
91 l/min) was homogenized by a Squid system.

92 A run of several unknowns was framed by analyses of GJ-1 as internal standard and of
93 three natural zircons (Temora, Plešovice and 91500) to monitor the external reproducibility.
94 Raw data were processed using Glitter software package (van Achtenberg et al., 2001), and
95 the Concordia age and diagram were obtained by Isoplot/Ex v. 4.15 (Ludwig, 2008). Repeated

96 measurements on the GJ-1 gave an age of 602.0 ± 2.7 Ma (2 sigma, n = 14) and the Plešovice
97 resultant age is 338.3 ± 2.2 Ma (2 sigma, n = 4), which is within error in the range of the
98 certified value (337.13 ± 0.37 Ma, Sláma et al. 2008).

99 Zircon grains extracted from the porphyritic monzogranite 13DB05 (see the following
100 section for the nomenclature) are pinkish, mostly of gem-quality, with few inclusions. They
101 are prismatic, elongated (2:1) and can reach length up to 250 microns. CL images reveal nice
102 oscillatory magmatic domains, sometimes convolute zones, with frequent inherited cores that
103 can be easily determined. Even with a careful selection of grains, most of the dating analyses
104 are not concordant and were thus disregarded (90% of our analyses). Roughly, half of these
105 discordant ages shows clearly mixing with inherited fraction, and the second half with
106 discordant young ages is affected by lead loss. For very few grains, the discordancy is so high
107 that it is more probably linked to analytical problems with the ^{207}Pb detection.

108

109 *2.2. Mineral and whole-rock analyses*

110

111 Mineral compositions were determined using a Cameca SX-100 electron microprobe
112 (Microsonde Ouest, Brest, France) with an acceleration voltage of 15kV, a beam current of
113 2nA and a beam diameter of 1 μm .

114 To get representative geochemical whole-rock analyses, at least 400 g of material for
115 fine-grained samples and 800 g for coarse-grained samples were prepared. A statistical
116 method of alternate shoveling was applied in view to homogenize the coarse gravel after a
117 first grinding (Pitard, 1993).

118 Whole-rock major and trace elements and isotopic ratios were determined at the
119 PSO/IUEM (Pôle Spectrométrie Océan, Institut Universitaire Européen de la Mer, Brest,
120 France). Major elements were analyzed by inductively coupled plasma-atomic emission

121 spectrometry (ICP-AES) using a Horiba Jobin Yvon® Ultima 2 spectrometer and following
122 the analytical procedure of Cotten et al. (1995). They were determined from an H₃BO₃
123 solution, boron being used as an internal standard. Relative standard deviations are < 2% (<
124 1% for SiO₂), except for low values (< 0.50 wt%), for which the absolute standard deviation
125 is ± 0.01 wt%. Trace elements were determined by high-resolution ICP-MS, using a Thermo
126 Element 2 spectrometer, following the sample preparation and analytical procedure described
127 by Barrat et al. (1996, 2000), who have developed a routine method using an ion-exchange
128 chromatography procedure. Aliquots of the mother solutions were spiked with a solution of
129 pure Tm and then evaporated to dryness. Relative standard deviations are < 5% for most of
130 trace elements and < 10% for Nb, Gd, Tb, Ta, Ni, Zn and Rb. Because of zircon resistance
131 against dissolution, a second method was tested to improve Zr and Hf concentrations in some
132 granitic samples. Thus, seven zircon-bearing samples were analyzed a second time by using
133 high pressure Teflon vessel bombs, in association with HClO₄, following the sample
134 preparation of Révillon and Hureau-Mazaudier (2009). However, this method was not
135 selected, as leading to erratic results for the rare earth elements, without any significant
136 changes in mean concentrations. Consequently, the Zr and Hf data presented here have to be
137 considered with caution and are not shown in any diagram.

138 Sr isotopic ratios were measured by thermal ionization mass spectrometry (TIMS),
139 while Nd isotopic ratios were determined using a multicollector ICP-MS (PSO/IFREMER,
140 Brest, France). The protocol for element separation is described in Richard et al. (1976) and
141 White and Patchett (1984).

142

143 **3. Geology**

144

145 *3.1. Regional context*

146
147
148
149
150
151
152
153
154
155
156
157
158
159
160
161
162
163
164
165
166
167
168
169
170

The Late Variscan development of the Armorican orogenic belt is dominated by large-scale strike-slip tectonics, coeval to 308-300 Ma-old synkinematic granitic intrusions along two ductile shear zones: the South Armorican dextral Shear Zone (Berthé et al., 1979), and the Plouguerneau-Guisseny sinistral Shear Zone (PGSZ), in the Leon Domain (Chauris, 1994). In the latter area, the Aber-Ildut/North-Ouessant complex roots to the north along the steeply-dipping and NE-/SW-striking PGSZ that extends further west along the two dextrally offset branches of the North Ouessant Shear Zone (NOSZ) (Fig. 1b, c) (Le Gall et al., 2014). It is a composite intrusion, comprising three submassifs, namely the North Ouessant (NO), the West Aber-Ildut (W-AI) and the East Aber-Ildut (E-AI) submassifs. The complex cuts through metamorphic and granitic terranes of the Léon Domain (Figs. 1a and b) (Ballèvre et al., 2009; Faure et al., 2010).

The earlier and polyphased tectono-metamorphic history of the Léon hosted terranes started in the time-range 440-340 Ma with a HP metamorphic event, coeval to northerly-directed thrusting during an early oceanic subduction to collision phase. The following stage (340-300 Ma) resulted in the exhumation of deeply-buried units associated with migmatites in HT metamorphic conditions during a transtensional, and locally pure transcurrent shear regime, synchronously to multistage granitic intrusions (Paquette et al., 1987; Schultz et al., 2007; Marcoux et al., 2009; Faure et al., 2010; Schultz, 2013; Le Gall et al., 2014). Dextral shearing along the North Armorican Shear Zone (NASZ) was accompanied by the intrusion of the 316.0 ± 2.0 Ma (U/Pb zircon ages) St-Renan-Kersaint synkinematic granite (Le Gall et al., 2014). This event just predated the c. 300 Ma magmatic and tectonic activities studied in this paper, assigned to late syn-convergence processes in response to a NS-directed shortening.

171 3.2 Sampling and nomenclature

172

173 Most samples were collected in the northern part of the Ouessant Island (NO, Fig. 1c)
174 and along the western coastal sector of the Aber-Ildut pluton (W-AI, Fig. 1d). Two additional
175 samples were taken in the eastern sector of the Aber-Ildut pluton (E-AI, Fig. 1b) and one
176 offshore sample (C34, Fig. 1b) was cored by gravity Cnexo-ville rock core (Le Gall et al.,
177 2014). In addition to magmatic rocks, two metasedimentary xenoliths (AI11 and AI27) were
178 sampled in the W-AI submassif (Fig. 1d).

179 Granitoid nomenclature is based on the Q' vs. ANOR diagram of Fig. 2, derived
180 empirically by Streckeisen and Le Maitre (1979) from the IUGS classification of Streckeisen
181 (1976) and considered as its CIPW normative equivalent. This diagram is based on the
182 normative parameters $100Q/(Q + Ab + Or + An)$, representing silica saturation, and
183 $100An/(An + Or)$ that reflects the relative abundance of calcium and potassium in the rocks.
184 Sample OS11, which plots in the lower part of the Afs granite field, displays a mineralogy of
185 Afs quartz microsyenite (see below) and, thus, will be considered as such. Lamprophyres are
186 classified by using the $CaO-SiO_2/10-4TiO_2$ diagram of Rock (1987) in Fig. 3. AI
187 lamprophyres plot in the calc-alkalic field.

188

189 3.3. Geochronology

190

191 The W-AI porphyritic monzogranite 13DB05 yielded a Concordia age of 303.8 ± 0.89
192 Ma (1 sigma, MSWD = 2.9), slightly older than its $^{206}Pb/^{238}U$ age of 302.8 ± 2.0 Ma (1 sigma,
193 MSWD = 0.56) (Supplementary Table S1 and Fig. 4). This Concordia age is consistent with
194 previously published ages of: 301.4 ± 4.3 Ma (U-Pb/TIMS) for the AI porphyritic
195 monzogranite (Marcoux et al., 2009); 292.6 ± 2.7 Ma (Ar/Ar) for the PGSZ mylonites

196 (Marcoux et al., 2009). These ages typically concern one of the latest Variscan events in the
197 Armorican Massif (see Ballèvre et al., 2009, for a review).

198

199 *3.4 Field relationships*

200

201 Granitoids located close to both the PGSZ and the NOSZ exhibit C/S-type tectonic
202 fabrics indicating ductile sinistral shearing. Away from the shear zones, granitoids are nearly
203 unstrained and still contain preserved magmatic flow structures outlined by Afs megacryst
204 orientation and elongated enclaves (Fig. 5a).

205 Porphyritic monzogranites (Fig. 5a, b, d) form the main part of the Aber-Ildut pluton,
206 since constituting two-thirds of the W-AI submassif (Fig. 1d), and cropping out locally in the
207 eastern sector (Fig. 1b). Porphyritic syenogranites occur in the southern sector of the W-AI
208 submassif, but not at its edge (Fig. 1d), and in the central part of the Ouessant Island (Fig. 1c).
209 Two-mica leucogranites are the prominent facies in the E-AI submassif (Fig. 1b). They also
210 occur as intrusive bodies of various sizes in the W-AI submassif (Fig. 1d). Mingling
211 structures, observed north of the W-AI submassif, reveal that the monzogranites have been
212 intruded by the leucogranites prior to their complete solidification. The northern part of
213 Ouessant is exclusively composed of two-mica leucogranites (Figs. 1c and 5c, e). Sample C34
214 confirms the extension of this facies offshore (Fig. 1b). Microgranites constitute a dense NS-
215 trending dyke network cutting through the central part of the W-AI submassif (Fig. 1d). They
216 are a few meters wide and can be up to 3 km long. The systematic presence of fine-grained
217 chilled margins typically attests that their emplacement postdates the crystallization of their
218 granitic host. Tourmaline-bearing leucogranites are exposed at the southern edge of the W-AI
219 submassif (Fig. 1d).

220 Very abundant ovoid quartz-monzodioritic or granodioritic enclaves are included in
221 monzo-/syenogranites in the W-AI submassif (Fig. 1d). In some cases, it can be noticed that
222 orthose megacrysts have migrated from the host granite into enclaves, hence demonstrating
223 that both granodiorites and quartz monzodiorites were liquid at the time of their incorporation
224 into granites (Fig. 5a). Along the NS coastal section, the orientation of elongated enclaves
225 changes southwards from a N70°E direction, i.e. parallel to the PGSZ, to a submeridian
226 orientation, i.e. nearly perpendicular to the PGSZ (Fig. 1d). Two large areas of quartz
227 monzodiorites, with mingling structures (Fig. 5c), are exposed in the Ouessant Island (Fig.
228 1c).

229 Two kinds of ultrapotassic dykes are identified in the AI-NO complex: calc-alkalic
230 lamprophyres in the W-AI submassif and alkali feldspar (Afs) quartz microsyenites in North-
231 Ouessant. Lamprophyric dykes are a few meters wide and can be up to several hundred
232 meters long (Fig. 5d). They have a NS direction, consistent with a submeridian compression
233 (Rolet et al., 1986). Their emplacement predates the end of crystallization of their monzo-
234 /syenogranitic host-rocks, as evidenced by the presence of mingling structures along the
235 contact. By contrast, in the North Ouessant area, unstrained dykes of Afs quartz microsyenites
236 postdate their sheared two-mica leucogranite host-rock.

237

238 **4. Petrology and mineralogy**

239

240 *4.1. Porphyritic monzogranites*

241

242 Porphyritic monzogranites are typically characterized by 35 x 15 mm-sized
243 (sometimes > 50 mm) red orthoclase megacrysts (Fig. 5b). Their color is probably due to iron
244 oxide impurities (Chauris, 1994). Quartz, andesine, apatite-bearing biotite, ilmenite and rare

245 titanite and zircon are also present. Muscovite and amphibole are lacking. Monzogranite
246 biotites plot at the boundary between calc-alkalic and peraluminous fields in the
247 discrimination diagram of Abdel-Rahman (1994) in Fig. 6a.

248

249 *4.2. Syenogranites*

250

251 To the naked eyes, porphyritic syenogranites resemble the previous monzogranite
252 facies. However, the orthoclase megacrysts are slightly smaller and generally colorless,
253 except in Ouessant, where they are red. The mineralogy of porphyritic syenogranites differs
254 from those of monzogranites with the oligoclase composition of its plagioclases, as well as
255 with the presence of very few muscovite crystals. The gradual transition from the porphyritic
256 monzogranitic facies into the syenogranitic one is part of the spatial magmatic zonation
257 leading progressively to the W-AI south border facies (Fig. 1d).

258 The two-mica syenogranites form a first peripheral strip in the southern part of the W-
259 AI submassif: they crop out south of the porphyritic syenogranites and in the southeastern
260 edge of the area (Fig. 1d). The corresponding rocks have a coarse texture and contain only
261 sparse orthoclase megacrysts. The muscovite/biotite ratio increases progressively southwards:
262 biotite is more abundant than muscovite in the northern part of the strip and the opposite is
263 true near the limit with the southern leucogranites (Chauris, 1994).

264 All syenogranite biotites plot in the peraluminous field in the Fig. 6a discrimination
265 diagram.

266

267 *4.3. Alkali feldspar leucogranites*

268

269 The two-mica (micro)leucogranites display varied petrographic facies (presence or not
270 of a few alkali feldspar megacrysts, coarse- versus fine-grained size, variable
271 muscovite/biotite ratio), but all of them are clear-colored and contain orthoclase or
272 microcline, quartz, oligoclase-albite, muscovite, biotite, apatite, and sometimes zircon.
273 Andalusite crystals have been identified in the sample AI19 (Supplementary Table S2). Late-
274 to post-magmatic tourmaline occurs as either disseminated cluster or tourmaline-filled veins.

275 Tourmaline leucogranites are very clear rocks containing dark tourmaline crystals,
276 often more than 1 cm long, disseminated in the groundmass. Note that the AI3a tourmalines
277 are more magnesian than the AI2 ones (Supplementary Table S2). The only other colored
278 mineral is poikilitic red garnet, a few millimeters in diameter (Fig. 5f). Its composition is
279 dominated by almandine (0.71 - 0.61) and spessartine (0.28 - 0.38) (Supplementary Table S2).
280 Biotite is lacking. Colorless minerals are microcline, albite, quartz and muscovite (Fig. 5f).
281 Near the AI2 sampling point (Fig. 1d), a greisen-type alteration results locally in newly-
282 formed quartz and muscovite (Chauris, 1994). Tourmaline and garnet are resistant to this
283 alteration.

284 All leucogranite biotites plot in the peraluminous field in Fig. 6a.

285

286 *4.4. Enclaves*

287

288 *4.4.1. Granodiorites and quartz monzodiorites*

289 The corresponding dark and fine-grained rocks contain plagioclase, quartz, orthose,
290 biotite, titanite, Fe-Ti oxides and minor apatite; green hornblende occurs in the quartz
291 monzodiorite OS1. Quartz monzodiorites only differ from granodiorites by their greater
292 plagioclase content, present as phenocrysts in the sample AI28. Biotites in the granodiorite
293 AI6b plot in the peraluminous field in Fig. 6a, near the boundary with the calc-alkalic field.

294

295 *4.4.2. Metasedimentary xenoliths*

296 Sample AI11 is a diatexite made up of large leucocratic veins (quartz, orthose,
297 plagioclase, muscovite, biotite and minor apatite), together with a diffuse restite network of
298 biotite-rich veinlets. Sample AI27 is an ancient pelitic rock recrystallized into hornfels. It is
299 composed of a fine-grained matrix of polygonal quartz, biotite and plagioclase, crossed by
300 thin coarse-grained leucocratic veins, containing perthitic orthoclase, quartz and subordinate
301 biotite. Muscovite is confined to some narrow zones, which might outline previous
302 sedimentary beds with different composition.

303

304 *4.5. Ultrapotassic dykes*

305

306 Lamprophyres are melanocratic hypabyssal igneous rocks with porphyritic fine-
307 grained textures carrying hydrous mafic phenocrysts (Rock, 1987, 1991). Feldspars are
308 generally restricted to the groundmass (Prelević et al, 2004). Calc-alkalic lamprophyres are
309 commonly associated with granites of same affinity. Aber-Ildut lamprophyres are mica-phyrlic
310 fine-grained rocks (Fig. 5g). The brown mica phenocrysts, up to 2 mm long, have a Mg-Ti-
311 rich biotite composition. They can form clusters, a few millimeters in diameter. Groundmass
312 micas are also biotites, or Fe-rich phlogopites, which have a less pronounced brown color.
313 Biotites plot in the calc-alkalic field in Fig. 6a; biotites and phlogopites plot in the calc-alkalic
314 lamprophyre fields in the discrimination diagrams of Rock (1987) in Fig. 6b. The other
315 primary phases are: orthoclase, which forms the main part of the groundmass, quartz,
316 sometimes corroded, rare plagioclase, augite-diopside, and apatite, quite abundant in the
317 groundmass, which also occurs in the form of 2 mm-long phenocrysts in a few samples.
318 Alteration is expressed by kaolinization of K-feldspars, partial chloritization of micas and

319 amygdale filling with quartz and epidote. These calc-alkalic lamprophyres have a minette-
320 type mineralogy (biotite phenocrysts and alkali feldspar dominant in the groundmass),
321 according to the criteria of Rock (1991) and Prelević et al. (2004).

322 Although the dyke sample OS11 plots in the alkali feldspar granite field (Fig. 2), its
323 mineralogy is rather consistent with that of an alkali feldspar quartz microsyenite. It is a
324 subaphyric cryptocrystalline rock. Small phenocrysts of orthose, chloritized biotite, sparse
325 altered oligoclase and euhedral apatite are immersed in a groundmass mainly made up of
326 orthose, quartz, and subordinate biotite and augite. Secondary quartz, sometimes surrounded
327 by chlorite needles, fills a few spherical amygdales.

328

329 **5. Geochemistry**

330

331 *5.1. Major elements*

332

333 All the AI-NO available major and trace element compositions are presented in Table
334 1. Among the four geochemical discrimination diagrams versus SiO₂ shown in Fig. 7, three of
335 them were used by Frost et al. (2001) in their classification scheme, whereas the fourth one is
336 the classical K₂O-SiO₂ diagram of Peccerillo and Taylor (1976).

337 The Fe* diagram in Fig. 7a can be used to distinguish ‘magnesian’ from ‘ferroan’
338 granitoids, as proposed by Frost et al. (2001). Samples that plot in the magnesian field have
339 not necessarily mole proportion of Mg higher than Fe, they are just relatively Mg enriched
340 compared with the whole population of granitoids. Following Frost et al. (2001), magnesian
341 compositions would be consistent with hydrous, oxidizing magmas. All the AI-NO analyzed
342 samples are magnesian, except one syenogranite and the more silicic leucogranites.

343 The MALI (modified alkali-lime index) diagram in Fig. 7b allows the characterization
344 of granitoid compositional series. With the exception of the ultrapotassic rocks and one
345 tourmaline leucogranite, all the AI-NO analyzed magmatic samples follow – or are very close
346 to – the alkali-calcic trend. This feature, also visible in the Q'-ANOR diagram in Fig. 2, has
347 been considered elsewhere as a specific attribute of post-tectonic Paleozoic granitoids in the
348 Irish and British Variscides (Frost et al., 2001).

349 The ASI (aluminium saturation index) diagram in Fig. 7c can be used to discriminate
350 peraluminous ($ASI > 1$) from metaluminous ($ASI < 1$; $Na + K < Al$) and peralkaline rocks
351 ($ASI < 1$; $Na + K > Al$). The expression of the ASI, including P_2O_5 (Fig. 7c), takes into
352 account the presence of apatite. If $ASI > 1.1$, rocks are considered as strongly peraluminous
353 (SP) (Sylvester, 1998). The SP granites are commonly thought to originate from a pure
354 sedimentary source (Sylvester, 1998; Frost et al., 2001). The whole set of the AI-NO analyzed
355 samples – except one lamprophyre and the NO quartz monzodiorite – is peraluminous; all the
356 leucogranites are strongly peraluminous, together with most of the syenogranites.
357 Peraluminosity increases roughly with SiO_2 .

358 The K_2O versus SiO_2 diagram in Fig. 7d shows that the AI-NO plutonic association
359 corresponds to a high-K/ultra-K magmatism. The Afs quartz microsyenite OS11 plots high
360 above the high-K/shoshonitic limit, together with the hornfelds AI27. Lamprophyres have
361 also very high K_2O contents (> 5 wt %) and plot in the calc-alkalic lamprophyre field of Rock
362 (1987).

363 The SiO_2 and MgO contents of the AI-NO calc-alkalic lamprophyres (55.5 – 57.3 and
364 3.6 – 3.8 wt%, respectively, Table 1) matches those of western Serbia leucominettes ($50.5 <$
365 $SiO_2 < 61.0$ wt%; $2.6 < MgO < 7.5$ wt%: Prelević et al., 2004). They are distinct from the
366 post-Variscan Mg-rich minettes of SW England ($48.0 < SiO_2 < 52.9$ wt%; $5.3 < MgO < 8.1$

367 wt%: Leat et al., 1987; see also Figs. 3 and 7d), despite similar geological context and age (c.
368 290 Ma).

369 Variations of MgO, Al₂O₃, and P₂O₅ relative to SiO₂ are rather regular from
370 leucominettes to leucogranites (Fig. 8a-c). It can be noticed that (1) the quartz monzodiorite
371 AI28 and the hornfels AI27 are enriched in Al₂O₃ (> 17 wt%) with respect to the other
372 samples; (2) the ultrapotassic rocks are especially enriched in P₂O₅, which reflects the
373 abundance in apatite; and (3) the Afs quartz microsyenite OS11 has a composition that plots
374 between the leucominettes and the porphyritic syenogranites.

375

376 5.2. Trace elements

377

378 A selection of trace elements having contrasted magmatic behaviors is shown in
379 function of SiO₂ in the diagrams in Fig. 8d-f. Except for the ultrapotassic rocks and the
380 metasedimentary xenoliths, the evolutionary trends of Ba, Eu and Y are fairly regular.
381 Leucominettes are characterized by high Y and Eu values, and more especially by huge Ba
382 contents (> 5000 ppm). The Afs quartz microsyenite displays geochemical features
383 comparable, but attenuated, to those of the lamprophyres.

384 AI-NO moderately peraluminous (MP) rocks (quartz monzodiorites, granodiorites and
385 monzogranites) are enriched in light and middle rare earth elements (LREE and MREE,
386 respectively) with respect to heavy REE (HREE). The corresponding distribution patterns are
387 very close to each other (Fig. 9a).

388 AI-NO strongly peraluminous (SP) granitoids (syenogranites – Fig. 9a – and
389 leucogranites – Fig. 9b) display lower REE patterns, with more marked Eu anomalies. Note
390 the remarkable resemblance between the patterns of OS4 (NO two-mica leucogranite) and
391 AI32 (W-AI two-mica microleucogranite), in agreement with the other geochemical diagrams

392 (Figs. 2, 7, 8). Compared with the two-mica rocks, the tourmaline leucogranites AI2 and AI3a
 393 are depleted in REE (except in Yb and Lu) and especially in Eu. In addition, their REE
 394 behavior does not gradually change into smooth curvilinear patterns, as usual, from La to Lu:
 395 the lanthanides can be subdivided into four groups with different pattern shapes, separated by
 396 slope breaks (Fig. 9b). In particular, groups 1 (La, Ce, Pr, Nd) and 3 (Gd, Tb, Dy, Ho) are
 397 characterized by the parallelism of the corresponding AI2 and AI3a concave-down curve
 398 sectors.

399

400 5.3. Isotopes

401

402 The Sr and Nd isotopic ratios are presented in Table 2. In the ϵ_{Nd}^t vs. initial $^{87}\text{Sr}/^{86}\text{Sr}$ (t
 403 = 304 Ma) diagram in Fig. 10a, there are clear relationships between the isotopic composition
 404 and the petrologic characteristics of the samples. The MP granitoid samples (AI6b and AI26)
 405 plot close to both the leucominette AI33 and the Afs quartz microsyenite OS11 ($0.705613 <$
 406 $^{87}\text{Sr}/^{86}\text{Sr}_i < 0.706609$; $-3.00 < \epsilon_{\text{Nd}}^{304} < -1.58$; Table 2); the SP leucogranitic samples have
 407 higher initial $^{87}\text{Sr}/^{86}\text{Sr}$ ratio and lower initial ϵ_{Nd} ($0.706538 < ^{87}\text{Sr}/^{86}\text{Sr}_i < 0.713548$; $-5.43 <$
 408 $\epsilon_{\text{Nd}}^{304} < -4.36$). The migmatite AI11 has a leucogranite-type isotopic composition ($^{87}\text{Sr}/^{86}\text{Sr}_i =$
 409 0.709571 ; $\epsilon_{\text{Nd}}^{304} = -5.29$); by contrast, the hornfels AI27 displays an original isotopic
 410 composition, with a high $^{87}\text{Sr}/^{86}\text{Sr}$ ratio (0.719068) and a very low $\epsilon_{\text{Nd}}^{304}$ of -12.17 (Table 2).
 411 The isotopic compositions of the AI-NO hornfels and leucogranites fit with those of pelites
 412 and peraluminous late-Variscan granites, respectively, from the Spanish Central Region (Fig.
 413 10a) (Villaseca et al., 1998).

414

415 6. Discussion

416

417 *6.1. Emplacement of the AI-NO complex*

418

419 The preferred orientation of quartz monzodiorite/granodiorite enclaves in the coastal
420 W-AI submassif (i.e., parallel to the PGSZ near the shear zone, perpendicular to the PGSZ
421 southwards, and randomly oriented close to the southern edge, Fig. 1d), once combined to the
422 petrological data presented in section 4, is consistent with the following two-stage
423 emplacement model previously applied by Jamgotchian (1986) and Chauris (1991, 1994) to
424 the AI pluton.

425 A first magmatic arrival rose through the PGSZ conduit, before injecting southward as
426 a huge horizontal sill (Fig. 11). The observed north-south compositional gradient implies that
427 tourmaline leucogranites were emplaced prior to syenogranites that in turn predate
428 monzogranites. As a first approximation, the progressive petrological transition, marked by a
429 noticeable muscovite enrichment southwards, could be consistent with the existence of a
430 stratified reservoir at depth, with leucocratic magmas at the top and monzogranitic (\pm Q-
431 monzo/granodioritic) liquids at the bottom. Another possibility would be to consider
432 disconnected evolution of heterogeneous liquids within different reservoirs, with magmas
433 using a same pathway when emplaced in the upper crust. A similar crustal ascent path through
434 the NOSZ can be envisaged for the Ouessant porphyritic syenogranite.

435 During the second stage, two-mica leucogranitic bodies were intruded along the
436 PGSZ/NOSZ, before the end of crystallization of the first injection. They currently form the
437 northern part of the W-AI pluton, nearly all the E-AI pluton, and the northern sector of
438 Ouessant. Field relationships suggest that the other occurrences of two-mica leucogranites,
439 such as C34- and AI5-type intrusions (Fig. 1b, d), could correspond to residual inliers of
440 eroded initially horizontal sill units, overlying syeno-/monzogranites that rooted further north
441 along the PGSZ/NOSZ (Fig. 11).

442 Finally, the AI-NO complex was intruded by three distinct dyke swarms comprising:
443 (1) leucominettes, emplaced before the end of crystallization of the previous units; (2) two-
444 mica microleucogranites, and (3) Afs quartz microsyenites, both postdating crystallization in
445 the plutonic complex.

446

447 *6.2. Petrogenesis of the SP/MP granitoids*

448

449 The proposed emplacement model for the AI-NO complex is consistent with one or
450 several reservoir(s) containing both strongly (SP) and moderately peraluminous (MP)
451 magmas, but it leads to questions about the source of these two types of magmas and the
452 possible genetic links between them.

453 Although fractional crystallization is a process invoked by several authors to explain
454 chemical variations in various granitic complexes (e.g., Cocherie et al., 1994; Ramírez and
455 Grundvig, 2000), such a mechanism is unsuitable in the AI-NO case, for two reasons: (1) pure
456 fractional crystallization is not consistent with variations of initial isotopic ratios (Fig. 10a),
457 and (2) subaluminous minerals (e.g., amphibole, apatite, titanite), likely to increase
458 peraluminosity in silicic residual liquids by fractionating, are either absent or rare in the
459 studied rocks.

460 Assimilation coupled with fractional crystallization (AFC) might be a key to resolve
461 these two problems. Indeed, crustal contamination might have caused both isotopic variations
462 and increase in the peraluminosity degree from MP to SP magmas. Results of Villaseca et al.
463 (1998) about Variscan granitic batholiths of Spanish Central Region (CSR), displaying Sr-Nd
464 isotopic compositions of both granitic and country rocks comparable to those of the AI-NO
465 complex (Fig. 10a), have shown that: (1) AFC modeling implies either an unrealistically high
466 mantle contribution (for a pelitic contamination) or an excessively elevated assimilation rate

467 (for a contamination with meta-igneous material), and (2) none of the metamorphic country
468 rocks has the appropriate isotopic composition to satisfy the origin of the granites. It has been
469 noted above about the AI metasedimentary samples that only the initial Sr-Nd isotopic
470 composition of the migmatite AI11 matches those of the strongly peraluminous AI-NO
471 granites (Fig. 10a). The hornfels AI 27 have a less radiogenic $^{143}\text{Nd}/^{144}\text{Nd}$ initial ratio and a
472 more radiogenic $^{87}\text{Sr}/^{86}\text{Sr}$ initial ratio than the granites (Fig. 10a). Consequently, it cannot be
473 regarded as a potential contaminant in an AFC model. Such a feature corresponds to that
474 described by Villaseca et al. (1998).

475 Most authors consider that SP granites strictly originate from crustal melting processes
476 (Sylvester, 1998; Ramírez and Grundvig, 2000; Frost et al., 2001; Eyal et al., 2004; Antunes
477 et al., 2008), whereas MP high-K calc-alkalic/alkali-calcic granites instead would result from
478 interaction between crustal- and mantle-derived melts (Wenzel et al., 1997; Rottura et al.,
479 1998; Sylvester, 1998; Patiño Douce, 1999; Eyal et al., 2004) (see section 6.5. for a detailed
480 discussion of this second point about AI-NO granitoids). In this way, Villaseca et al. (1998)
481 have proposed a crustal-derived model, with limited-scale mixing between mafic and felsic
482 magmas, to account for the genesis of the Central Spain SP/MP peraluminous granites. To
483 explain the isotopic difference between metapelites and granites, they considered the
484 possibility of disequilibrium partial melting in high-grade anatectic areas. Indeed, Barbero et
485 al. (1995) showed that the pelite-derived anatectic leucogranites from Toledo (Spain) have
486 systematically higher initial ϵ_{Nd} and lower initial $^{87}\text{Sr}/^{86}\text{Sr}$ than the regional unmelted
487 metapelites. Such initial isotopic differences between a protolith and its melted products are
488 thought to be controlled by both the kinetic of the melting and the stoichiometry of the
489 reaction (Hammouda et al., 1994). Following Barbero et al. (1995) and Villaseca et al. (1998),
490 the differences would result from an enrichment in biotite and accessory minerals of the
491 migmatitic mesosomes, relative to the leucosomes during partial melting (Fig. 10b). In the AI-

492 NO complex under study, the isotopic difference observed between the slightly melted
493 metapelitic hornfels AI27 and the leucosome-rich migmatite AI11 could be satisfactorily
494 explained by such an isotopic disequilibrium model (arrow in Fig. 10a). Consequently, in
495 spite of their contrasted initial isotopic composition, the couple AI11/AI27 could be a good
496 candidate for matching the – probably heterogeneous – protolith of the AI-NO strongly
497 peraluminous leucogranites.

498

499 *6.3. Tetrad effect in leucogranites*

500

501 The tetrad effect, first defined by Peppard et al. (1969), reflects a process affecting the
502 REE complexing behavior (Bau, 1997; Irber, 1999). Masuda et al. (1987) described concave-
503 down tetrad REE patterns in extracted magmatic liquids. Since then, such specific REE
504 patterns have been observed in several highly silicic granites (Bau, 1997; Irber, 1999; Jahn et
505 al., 2001). In chondrite-normalized REE diagrams, the tetrad effect is readily identifiable by
506 the presence of four sectors of four elements separated at three positions: between Nd and Pm;
507 at Gd; and between Ho and Er. The tetrad effect is generally accompanied by modified
508 geochemical behavior of many non-REE trace elements, leading to variations in ratios known
509 to remain constant, such as K/Rb, K/Ba or Zr/Hf (Irber, 1999; Jahn et al., 2001).

510 REE patterns of the two W-AI tourmaline leucogranites seem to reveal a tetrad effect,
511 with the individualization of four sectors, numbered from 1 to 4 in Fig. 9b. To test this
512 hypothesis, and also to find out if that process affects other AI-NO granites, we have plotted
513 in Fig. 12 two diagrams with trace element ratios known to be sensitive to tetrad effect (K/Ba
514 and Eu/Eu*) in function of the parameter $TE_{1,3}$ of Irber (1999). The latter expression,
515 developed in Table 1, can be used to quantify the degree of tetrad effect on the first and third
516 REE tetrads, where the phenomenon is generally most obvious. K/Ba is positively correlated

517 with $TE_{1,3}$ (Fig. 12a), whereas Eu/Eu^* is negatively correlated (Fig. 12b). The latter diagram
518 shows clear correlation between magnitude of the Eu anomaly and the degree of tetrad effect.
519 It follows that the tetrad effect concerns, to a varying degree, all the AI-NO granites, all the
520 more so as they are silicic.

521 The tetrad effect reflects the influence of chemical complexation. It is commonly
522 interpreted as the result of the opening of a magmatic system at the ultimate stages of its
523 evolution, with intense interaction of the residual melts with F- and Cl-rich aqueous
524 hydrothermal fluids (Irber, 1999; Jahn et al., 2001). In the AI pluton, it might be in relation
525 with the greisen alteration observed close to the AI2 sampling point.

526

527 *6.4. Origin of the ultrapotassic rocks*

528

529 The origin of the calc-alkalic lamprophyres is still a matter of debate. However, there
530 is consensus to consider minettes as representing small-degree melts that form within the
531 lithospheric mantle at depths ≥ 50 km (Rogers et al., 1982; Wyman and Kerrich, 1993). Their
532 unusual geochemistry is generally explained by partial melting of a lithospheric mantle source
533 metasomatized by fluids derived from subducted material (Carmichael et al., 1996; Wenzel et
534 al., 1997; Hoch et al., 2001). More felsic minettes or leucominettes have been interpreted by
535 Prelević et al. (2004) as the result of hybridization between crustal-derived dacite-type
536 magmas and mantle-derived lamproitic melts, an idea previously put forward by Rock (1991).
537 Following Prelević et al. (2004), such a mixing mechanism is thought to be universally
538 applicable to the origin of (leuco)minettes associated with granites in late- or post-orogenic
539 settings.

540 The isotopic composition of the leucominette AI33, close to that of the granodiorites
541 and the monzogranites (Fig. 10a), is neither purely mantellic (i.e. with positive ϵ_{Nd}^t) nor

542 purely crustal (i.e. close to the SP granite composition). This feature suggests that
543 leucominettes likely result from mixing – or interaction – between crustal- and mantle-derived
544 products, in agreement with the model of Prelević et al. (2004).

545 In many diagrams in Fig. 8, the Afs quartz microsyenite OS11 plots in lines linking
546 leucominettes and porphyritic syenogranites. To check the hypothesis that OS11 resulted from
547 a mixing between these two magmatic types, a mass balance calculation test on major
548 elements (least-square approach of Wright and Doherty, 1970) has been performed with the
549 porphyritic syenogranite AI7 and the leucominette 13DB07. This test indicates that OS11
550 possibly originates by mixing 46.6 % of AI7 with 53.4 % of 13BD07 (sum of the squared
551 residuals $\Sigma R^2 = 1.03$, with weighting factors of 0.5 for CaO and K₂O). Such a model is
552 consistent with the isotopic similarity between the leucominette AI33, the monzogranite AI26
553 – the syenogranite AI7, not analyzed for isotopes, is thought to have a similar isotopic
554 composition – and OS11 (Fig. 10a). Nevertheless, additional fractionation/accumulation of
555 MREE-bearing minerals (such as apatite) is required to account for the respective shapes of
556 AI7 and OS11 REE patterns (Fig. 9b).

557

558 *6.5. Multistage mixing*

559

560 It has been argued in section 6.4. that the AI leucominettes might result from
561 hybridization between crustal- and mantle-derived materials, probably between SP-type and
562 lamproitic melts (Prelević et al., 2004). In addition, the NO Afs quartz microsyenite OS11 is
563 interpreted as the mixing product of syenogranitic and lamprophyric magmas. Finally, many
564 authors suggested that MP calc-alkalic/alkali-calcic granites also result from interaction
565 between crustal- and mantle-derived melts (Patiño Douce, 1999; Eyal et al., 2004).

566 In order to address these several mixing hypotheses, the AI-NO data are plotted in
567 Patiño Douce's (1999) diagrams, together with field contours of various peraluminous
568 granites and experimental curves (Fig. 13), and in Sylvester's (1998) diagrams, especially
569 devoted to SP granites (Fig. 14), where calculated curves are also indicated.

570 In Fig. 13 diagrams, the AI-NO SP granites plot into the leucocratic field of Patiño
571 Douce (1999), whereas the AI-NO MP granitoids fit with S-type granites. In the three
572 diagrams in Fig. 13, mafic pelites are located near the intersection of leucocratic and S-type
573 fields (Patiño Douce, 1999). The reaction curves model the melt compositions produced by
574 hybridization of olivine tholeiite with metapelite both at high (1.2-1.5 GPa) and low pressures
575 (< 0.5 GPa). These diagrams imply that: (i) the AI-NO SP leucogranites have a crustal origin,
576 perhaps pelitic; (ii) if the metasedimentary xenoliths AI11 and AI27 represent really the
577 protolith, as suggested by their isotopic compositions in Fig. 10a, their major element
578 chemistry has apparently been slightly modified during melting and metamorphism; (iii) the
579 AI-NO MP granitoids – plus leucominettes and OS11 – can result from mixing between
580 pelitic-derived melt(s) and mafic liquid(s); (iv) mixing occurs at low pressures (≤ 0.5 GPa)
581 (Fig. 13b, c).

582 The $\text{CaO}/\text{Na}_2\text{O}$ vs. $\text{Al}_2\text{O}_3/\text{TiO}_2$ diagram in Fig. 14a shows the late-orogenic SP
583 granites field defined by Sylvester (1998), together with a mixing curve between basalt and
584 pelite-derived melt (see Fig. 14a for more details). All the AI-NO syeno- and leucogranites
585 plot within the Sylvester's (1998) SP field, except the tourmaline-leucogranites. The AI-NO
586 MP granitoid field, to which can be added leucominettes and OS11, extends parallel to the
587 mixing curve, slightly shifted to the left. This feature can be interpreted as indicating that the
588 AI-NO MP granitoids result from mixing between both pelite-derived melts and mafic
589 magmas slightly different from those used for the modeling. By contrast, the AI-NO MP data
590 fit perfectly with the calculated mixing curve between similar components in the Rb/Ba vs.

591 Rb/Sr diagram in Fig. 14b. Note that leucominettes plot just near the basalt end-member. The
592 most probable source for the AI-NO SP granites is clay-rich pelitic materials. Tourmaline-
593 leucogranites display very high Rb/Sr and Rb/Ba ratios, probably in response to the tetrad
594 effect, which affects them (Fig. 12). The migmatite AI11 plots very close to the calculated
595 pelite-derived melt.

596 Analyzing the diagrams in Figs. 13 and 14 confirms that the geochemical diversity of
597 the AI-NO granitoid complex likely results from mixing of different end-members material
598 comprising (1) a clay-rich pelitic (crustal) component, (2) mantle-derived lamproitic, and/or
599 (3) mafic melts. In any case, mantle metasomatism is a plausible mechanism to explain the
600 genesis of fluid-rich lamprophyric products – i.e. unsampled lamproites and/or mafic
601 minettes, thought to be at the origin of the analyzed leucominettes by hybridization with
602 crustal liquids. Late-orogenic AI-NO granitoids probably formed at low pressure (Figs. 13b
603 and c), in agreement with metamorphic and structural data indicating that, at 330-290 Ma, the
604 Leon Domain is the locus of strong crustal exhumation and transtension (Schulz et al., 2007;
605 Le Gall et al., 2014). These granitoids are thus produced by lithospheric thinning with
606 advective heating of a ≤ 50 km-thick crust from hot metasomatized asthenosphere (Sylvester,
607 1998) (Fig. 15). As underlined by Patiño Douce (1999), the nature of the chemical
608 interactions between the continental crust and invading mafic magmas is probably complex,
609 and assimilation, fractional crystallization, crystal accumulation and fluid transfer processes
610 might have interfered in addition to multistage magma mixing.

611

612 **7. Conclusions**

613

614 1. The late-Variscan Aber-Ildut/North-Ouessant (AI-NO) complex is an association of
615 late-orogenic high-K alkali-calcic granitoids dated at 303.8 ± 0.89 Ma. It comprises an early

616 magmatic intrusion that rooted vertically along the PGSZ/NOSZ conduit, before being
617 injected southwards as a huge horizontal zoned sill. A progressive enrichment in muscovite
618 southwards can be noted. A second magmatic stage resulted in the intrusion of a large
619 leucogranitic body, prior to the end of crystallization of the first injection. During a last stage,
620 the complex is intruded by three dyke swarms of leucominette, microleucogranite and quartz
621 microsyenite.

622 2. The main petrogenetic processes at the origin of the various petrographic types
623 sampled in the AI-NO complex are melting of crustal clay-rich pelitic material and mixing of
624 the resulting magmas with mantle-derived products. The strongly peraluminous (SP) granites
625 are interpreted as pure melting products. All the other petrographic types (moderately
626 peraluminous granitoids, leucominettes and quartz microsyenites) are thought to result from
627 mixing between crustal melts and mantle-derived mafic liquids. The more silicic granites
628 were affected by a tetrad effect, in relation with REE complexing behavior.

629 3. AI-NO granitoids probably formed at low pressure, during the Variscan late-
630 orogenic stage associated with exhumation, transtension, HT metamorphism and lithospheric
631 thinning, by advective heating of a ≤ 50 km-thick crust from hot metasomatized
632 asthenosphere.

633

634 Supplementary data to this article can be found online at...

635

636 **Acknowledgements**

637 Field studies were conducted in 2013 and 2014. Detailed and constructive comments
638 by two anonymous reviewers helped us to improve the text. The authors are grateful to J.
639 Langlade (microprobe analyses), C. Bollinger (ICP-MS Brest), P. Nonnotte (TI-MS), C.
640 Liorzou (ICP-AES), M.-L. Rouget (chemistry lab assistant, UMS n°3113), A. von Quadt

641 (U/Pb geochronology, ETH Zurich), P. Vonlanthen (Scanning electron microscopy, Institut
642 des Sciences de la Terre, Lausanne), P. Tieffenbach (thin sections), and J.-P. Oldra (sample
643 preparation). DBG has benefited from a Swiss National Science Foundation (SNSF) grant no.
644 PA00P2-145309. Many thanks to J.-A. Barrat for having detected the tetrad effect.

645

646 **References**

647

648 Abdel-Rahman, A.M., 1994. Nature of biotites from alkaline, calc-alkalic, and peraluminous
649 magmas. *Journal of Petrology* 35, 525-541.

650 Antunes, I.M.H.R., Neiva, A.M.R., Silva, M.M.V.G., Corfu, F., 2008. Geochemistry of S-
651 type granitic rocks from the reversely zoned Castelo Branco pluton (central Portugal).
652 *Lithos* 103, 445-465.

653 Ballèvre, M., Bosse, V., Ducassou, C., Pitra, P., 2009. Paleozoic history of the Armorican
654 Massif. Models for the tectonic evolution of the suture zones. *Comptes Rendus*
655 *Geoscience* 341, 174-201.

656 Barbarin, B., 1999. A review of the relationships between granitoid types, their origins and
657 their geodynamic environments. *Lithos* 46, 605-626.

658 Barbero, L., Villaseca, C., Rogers, G., Brown, P.E., 1995. Geochemical and isotopic
659 disequilibrium in crustal melting: An insight from the anatectic granitoids from Toledo,
660 Spain. *Journal of Geophysical Research* 100, 15 745-15 765.

661 Barrat, J.A., Blichert-Toft, J., Gillet, Ph., Keller, F., 2000. The differentiation of eucrites: The
662 role of *in situ* crystallization. *Meteoritics and Planetary Science* 35, 1087-1100.

663 Barrat, J.A., Keller, F., Amossé, J., Taylor, R.N., Nesbitt, R.W., Hirata, T., 1996.

664 Determination of rare earth elements in sixteen silicate reference samples by ICP-MS
665 after Tm addition and ion exchange separation. *Geostandards Newsletter* 20, 133-139.

- 666 Barrat, J.A., Zanda, B., Moynier, F., Bollinger, C., Liorzou, C., Bayon, G., 2012.
667 Geochemistry of CI chondrites: Major and trace elements, and Cu and Zn isotopes.
668 *Geochimica et Cosmochimica Acta* 83, 79-92.
- 669 Bau, M., 1997. The lanthanide tetrad effect in highly evolved felsic igneous rocks – A reply to
670 the comment by Y. Pan. *Contributions to Mineralogy and Petrology* 128, 409-412.
- 671 Berthé, D., Choukroune, P., Jegouzo, P., 1979. Orthogneiss, mylonite and non coaxial
672 deformation of granites : the example of the South Armorican Shear Zone. *Journal of*
673 *Structural Geology* 1, 31-42.
- 674 Carmichael, I.S.E., Lange, R.A., Luhr, J.F., 1996. Quaternary minettes and associated
675 volcanic rocks of Mascota, western Mexico: a consequence of plate extension above a
676 subduction modified mantle wedge. *Contributions to Mineralogy and Petrology* 124,
677 302-333.
- 678 Chappell, B.W., White, A.J.R., 1974. Two contrasting granite types. *Pacific Geology* 8, 173-
679 174.
- 680 Chauris, L., 1991. Le granite à tourmaline de Plouarzel (Finistère) : aspects chimico-
681 minéralogiques d'une différenciation marginale leucogranitique. *Géologie de la France*
682 4, 31-38 (in French).
- 683 Chauris, L., 1994. Notice explicative, Carte géologique de la France (1/50 000), feuille
684 Plouarzel-île d'Ouessant (237). Orléans, BRGM Éditions, 132 p. (in French).
- 685 Chauris, L., Hallégouët, B., 1989. Notice explicative, Carte géologique de la France (1/50
686 000), feuille Le Conquet (273). Orléans, BRGM Éditions, 69 p. (in French).
- 687 Cocherie, A., Rossi, P., Fouillac, A.M., Vidal, P., 1994. Crust and mantle contribution to
688 granite genesis. An example from the Variscan batholith of Corsica, France, studied by
689 trace-element and Nd–Sr–O-isotope systematics. *Chemical Geology* 115, 173-211.

- 690 Condie, K.C., 1993. Chemical composition and evolution of the upper continental crust:
691 contrasting results from surface samples and shales. *Chemical Geology* 104, 1-37.
- 692 Cotten, J., Le Dez, A., Bau, M., Caroff, M., Maury, R., Dulski, P., Fourcade, S., Bohn, M.,
693 Brousse, R., 1995. Origin of rare-earth element and yttrium enrichments in subaerial
694 exposed basalts: evidence from French Polynesia. *Chemical Geology* 119, 115-138.
- 695 Downes, H., Duthou, J.L., 1988. Isotopic and trace element arguments for the lower-crustal
696 origin of Hercynian granitoids and pre-Hercynian orthogneisses, Massif Central
697 (France). *Chemical Geology* 68, 291-308.
- 698 Eyal, M., Litvinovsky, B.A., Katzir, Y., Zandvilevich, A.N., 2004. The Pan-African high-K
699 calc-alkalic peraluminous Elat granite from southern Israel: geology, geochemistry and
700 petrogenesis. *Journal of African Earth Sciences* 40, 115-136.
- 701 Faure, M., Sommers, C., Melleton, J., Cocherie, A., Lautout, O., 2010. The Léon domain
702 (French Massif armoricain): a westward extension of the Mid-German Crystalline Rise?
703 Structural and geochronological insights. *International Journal of Earth Sciences* 99, 65-
704 81.
- 705 Frost, B.R., Barnes, C.G., Collins, W.J., Arculus, R.J., Ellis, D.J., Frost, C.D., 2001. A
706 geochemical classification for granitic rocks. *Journal of Petrology* 42, 2033-2048.
- 707 Hammouda, T, Pichavant, M., Chaussidon, M., 1994. Mechanism of isotopic equilibration
708 during partial melting : an experimental test of the behaviour of Sr. *Mineralogical*
709 *Magazine A* 58, 368-369.
- 710 Hoch M., Rehkämper, M., Tobschall, H.J., 2001. Sr, Nd, Pb and O isotopes of minettes from
711 Schirmacher Oasis, East Antarctica: a case of mantle metasomatism involving
712 subducted continental material. *Journal of Petrology* 42, 1387-1400.

- 713 Irber, W., 1999. The lanthanide tetrad effect and its correlation with K/Rb, Eu/Eu*, Sr/Eu,
714 Y/Ho, and Zr/Hf of evolving peraluminous granite suites. *Geochimica et Cosmochimica*
715 *Acta* 63, 489-508.
- 716 Jahn, B.M., Wu, F., Capdevila, R., Martineau, F., Zhao, Z., Wang, Y., 2001. Highly evolved
717 juvenile granites with tetrad REE patterns: the Woduhe and Baerzhe granites from the
718 Great Xing'an Mountains in NE China. *Lithos* 59, 171-198.
- 719 Jamgotchian, A., 1986. Interférences d'effets cisailants tangentiel et transcurrent: la mise en
720 place syntectonique du pluton granitique de l'Aber-Ildut (Nord-Finistère). Rennes,
721 Université de Rennes 1, Mémoire de DEA, 75 p. (in French).
- 722 Leat, P.T., Thompson, R.N., Morrison, M.A., Hendry, G.L., Trayhorn, S.C., 1987.
723 Geodynamic significance of post-Variscan intrusive and extrusive potassic magmatism
724 in SW England. *Transactions of the Royal Society of Edinburgh: Earth Sciences* 77,
725 349-360.
- 726 Le Gall, B., Authemayou, C., Ehrhold, A., Paquette, J.-L., Bussien, D., Chazot, G., Aouizerat,
727 A., Pastol, Y., 2014. LiDAR offshore structural mapping and U/Pb zircon/monazite
728 dating of Variscan strain in the Leon metamorphic domain, NW Brittany.
729 *Tectonophysics* 630, 236-250.
- 730 Leutwein, F., Chauris, L., Sonet, J., Zimmermann, J.L., 1969. Études géochronologiques et
731 géotectoniques dans le Nord-Finistère (Massif armoricain). *Sciences de la Terre, Nancy*
732 XIV, 329-358 (in French).
- 733 Ludwig, K. R., 2008. User's manual for Isoplot 3.70, a geochronological toolkit for Microsoft
734 Excel. Berkeley Geochronology Center Special Publication 4.
- 735 Maniar, P.D., Piccoli, P.M., 1989. Tectonic discrimination of granitoids. *Geological Society*
736 *of America Bulletin* 101, 635-643.

- 737 Marcoux, E., Cocherie, A., Ruffet, G., Darboux, J.R., Guerrot, C., 2009. Géochronologie
738 revisitée du dôme du Léon (Massif armoricain, France). *Géologie de la France* 1, 19-40
739 (in French).
- 740 Masuda, A., Kawakami, O., Dohmoto, Y., Takenaka, T., 1987. Lanthanide tetrad effects in
741 nature: Two mutually opposite types W and M. *Geochemical Journal* 21, 199-124.
- 742 Middlemost, E.A.K., 1989. Iron oxidation ratios, norms and the classification of volcanic
743 rocks. *Chemical Geology* 77, 19-26.
- 744 Paquette, J.L., Balé, P., Ballèvre, M., Georget, Y., 1987. Géochronologie et géochimie des
745 éclogites du Léon : nouvelles contraintes sur l'évolution géodynamique du Nord-Ouest
746 du Massif armoricain. *Bulletin of Mineralogy* 110, 683-696 (in French).
- 747 Patiño Douce, A.E., 1995. Experimental generation of hybrid silicic melts by reaction of high-
748 Al basalt with metamorphic rocks. *Journal of Geophysical Research* 100, 15623-15639.
- 749 Patiño Douce, A.E., 1999. What do experiments tell us about the relative contributions of
750 crust and mantle to the origin of granitic magmas? In: Castro, A., Fernandez, C.,
751 Vigneresse, J.L. (Eds.), *Understanding granites. Integrating New and Classical*
752 *Techniques*. Geological Society, London, Special Publication 158, 55-75.
- 753 Patiño Douce, A.E., Johnston, A.D., 1991. Phase equilibria and melt productivity in the pelitic
754 system: implication for the origin of peraluminous granitoids and aluminous granulites.
755 *Contributions to Mineralogy and Petrology* 107, 202-218.
- 756 Peccerillo, A., Taylor, S.R., 1976. Geochemistry of Eocene calc-alkalic volcanic rocks from
757 the Kastamonu area. Northern Turkey. *Contribution to Mineralogy and Petrology* 58,
758 63-81.
- 759 Peppard, D.F., Mason, G.W., Lewey, S., 1969. A tetrad effect in the liquid-liquid extraction
760 ordering of lanthanides (III). *Journal of Inorganic and Nuclear Chemistry* 31, 2271-
761 2272.

- 762 Pitard, F.F., 1993. Pierre Gy's sampling theory and sampling practice: heterogeneity,
763 sampling correctness, and statistical process control, 2nd ed. CRC Press.
- 764 Prelević, D., Foley, S.F., Cvetković, V., Romer, R.L., 2004. Origin of minette by mixing of
765 lamproite and dacite magmas in Veliki Majdan, Serbia. *Journal of Petrology* 45, 759-
766 792.
- 767 Ramírez, J.A., Grundvig, S., 2000. Causes of geochemical diversity in peraluminous granitic
768 plutons: the Jálama pluton, Central-Iberian Zone (Spain and Portugal). *Lithos* 50, 171-
769 190.
- 770 Révillon, S., Hureau-Mazaudier, D., 2009. Improvements in digestion protocols for trace
771 element and isotope determinations in stream and lake sediment reference materials
772 (JSd-1, JSd-2, JSd-3, JLk-1 and LKSD-1). *Geostandards and Geoanalytical Research*
773 33, 397-413.
- 774 Richard, P., Shimizu, N., Allègre, C.J., 1976. $^{143}\text{Nd}/^{146}\text{Nd}$, a natural tracer: an application to
775 oceanic basalts. *Earth and Planetary Science Letters* 31, 269-278.
- 776 Rock, N.M.S., 1987. The nature and origin of lamprophyres: an overview, in: Fitton, J.G.,
777 Upton, B.G.J. (Eds.), *Alkaline Igneous Rocks*. Geological Society Special Publications,
778 30. Geological Society of London, United Kingdom, pp. 191-226.
- 779 Rock, N.M.S., 1991. *Lamprophyres*. Blackie and Son Ltd., Glasgow-London, United
780 Kingdom, p. 285.
- 781 Rogers, N.W., Bachinski, S.W., Henderson, P., Parry, S.J., 1982. Origin of potash-rich basic
782 lamprophyres: trace element data from Arizona minettes. *Earth and Planetary Science*
783 *Letters* 57, 305-312.
- 784 Rolet, J., Le Gall, B., Darboux, J.R., Thonon, P., Gravelle, M., 1986. L'évolution
785 géodynamique dévono-carbonifère de l'extrémité occidentale de la chaîne hercynienne

- 786 d'Europe sur le transect Armorique-Cornwall. Bulletin de la Société Géologique de
787 France 8, 43-54 (in French).
- 788 Rottura, A., Bargossi, G.M., Caggianelli, A., Del Moro, A., Visonà, D., Tranne, C.A., 1998.
789 Origin and significance of the Permian high-K calc-alkalic magmatism in the central-
790 eastern Southern Alps, Italy. Lithos 45, 329-348.
- 791 Schulz, B., Krenn, E., Finger, F., Bratz, H., Klemd, R., 2007. Cadomian and Variscan
792 metamorphic events in the Leon Domain (Armorican massif, France): P-T data and
793 EMP monazite dating, in: Linneman, U., Nance, R., Kraft, P. (Eds), The evolution of the
794 Rheic ocean from Avalonian-Cadomian active margin to Alleghenian-Variscan
795 collision. Geological Society of America Special Papers 423, 267-285.
- 796 Sláma, J. and 13 other authors. Plešovice zircon – A new natural reference material for U–Pb
797 and Hf isotopic microanalysis. Chemical Geology 249, 1-35.
- 798 Streckeisen, A.L., 1976. To each plutonic rock its proper name. Earth Science Reviews 12, 1-
799 33.
- 800 Streckeisen, A.L., Le Maitre, R.W., 1979. A chemical approximation to the modal QAPF
801 classification of the igneous rocks. Neues Jahrbuch für Mineralogie, Abhandlungen 136,
802 169-206.
- 803 Sylvester, P.J., 1998. Post-collisional strongly peraluminous granites. Lithos 45, 29-44.
- 804 Turpin, L., Cuney, M., Friedrich, M., Bouchez, J.L., Aubertin, M., 1990. Meta-igneous origin
805 of Hercynian peraluminous granites in the NW French Massif Central: implications for
806 crustal history reconstructions. Contributions to Mineralogy and Petrology 118, 13-32.
- 807 van Achterberg, E., Ryan, C.G., Jackson, S.E., Griffin, W., 2001. Data reduction software for
808 LA-ICP-MS, in: Sylvester, P. (Ed.), Laser Ablation- ICPMS in the Earth Science:
809 Principles and Applications. Mineralogical Association of Canada, Short Course Series,
810 Ottawa, Ontario, Canada, 29, pp. 239-243.

- 811 Villaseca, C., Barbero, L., Rogers, G., 1998. Crustal origin of Hercynian peraluminous
812 granitic batholiths of Central Spain: petrological, geochemical and isotopic (Sr, Nd)
813 constraints. *Lithos* 43, 55-79.
- 814 Wenzel, Th., Mertz, D.F., Oberhänsli, R., Becker, T., Renne, P.R., 1997. Age, geodynamic
815 setting, and mantle enrichment processes of a K-rich intrusion from the Meissen massif
816 (northern Bohemian massif) and implications for related occurrences from the mid-
817 European Hercynian. *Geologische Rundschau* 86, 556-570.
- 818 Whalen, J.B., Frost, C., 2013. The Q-ANOR diagram: a tool for the petrogenetic and
819 tectonomagmatic characterization of granitic suites. *Geological Society of America*
820 *Abstracts with Programs* 45, p. 24.
- 821 White, W.M., Patchett, J., 1984. Hf-Nd-Sr isotopes and incompatible element abundances in
822 island Arcs: implications for magma origins and crust-mantle evolution. *Earth and*
823 *Planetary Sciences Letters* 67, 167-185.
- 824 Wright, T.L., Doherty, P.C., 1970. A linear programming and least squares computer method
825 for solving petrologic mixing problems. *Geological Society of America Bulletin* 81,
826 1995-2008.
- 827 Wyman, D.A., Kerrich, R., 1993. Archean shoshonitic lamprophyres of the Abitibi
828 Subprovince, Canada: petrogenesis, age, and tectonic setting. *Journal of Petrology* 34,
829 1067-1109.
- 830 Zen, E-an, 1986. Aluminium enrichment in silicate melts by fractional crystallization: Some
831 mineralogic and petrographic constraints. *Journal of Petrology* 27, 1095-1117.

832

833 **Figure captions**

834

835 Fig. 1. Geological features of the Aber-Ildut/Nord-Ouessant (AI-NO) complex with sample
836 location (black and white dot) and name. (a) Location of the AI-NO complex within the
837 shear-zone patterns in the Armorican Massif. (b) Sketch geological map of the AI-NO
838 complex. Outline of the continental geological formations is from Chauris and Hallégouët
839 (1989) and Chauris (1994). Offshore formations are based on Chauris and Hallégouët (1989)
840 and Le Gall et al. (2014), and modified by taking the new data into account. W-AI: western
841 sector of the Aber-Ildut pluton; E-AI: eastern sector of the Aber-Ildut pluton; NO: North-
842 Ouessant submassif; PGSZ, NASZ, NOSZ: Porspoder-Guissény, North Armorican and North-
843 Ouessant Shear Zone, respectively. (c) Detailed geological map of North-Ouessant. (d)
844 Detailed geological map of the W-AI submassif.

845

846 Fig. 2. Q' vs. ANOR diagram for the AI-NO granitoids (Streckeisen and Le Maitre, 1979),
847 considered as a CIPW normative equivalent to the IUGS classification of Streckeisen (1976).
848 The suite trends of Whalen and Frost (2013), corresponding to the four plutonic rock series
849 defined by Frost et al. (2001) in their MALI (modified alkali-lime index) diagram (see Fig.
850 7b), are also indicated. CIPW norms have been calculated with $\text{Fe}_2\text{O}_3/\text{FeO} = 0.5$
851 (Middlemost, 1989).

852

853 Fig. 3. Triangular $\text{CaO-SiO}_2/10-4\text{TiO}_2$ plot of Rock (1987), discriminating the whole-rock
854 compositional fields of alkaline and calc-alkalic lamprophyres (AL and CAL, respectively).
855 The AI-NO ultrapotassic dykes are plotted and compared with the compositional fields of AI-
856 NO granitoids and minettes from SW England (Leat et al., 1987). Symbols as in Fig. 2.

857

858 Fig. 4. U-Pb geochronologic results of the AI monzogranite 13DB05, all given with errors at
 859 1 sigma level (ellipses and error bars): a) Concordia diagram with the resultant age (grey
 860 ellipse and framed age); b) weighted average $^{206}\text{Pb}/^{238}\text{U}$ age.

861
 862 Fig. 5. Photographs and photomicrographs of various types of rocks from the AI-NO
 863 complex. (a) Ovoid granodioritic enclave in the porphyritic monzogranite (W-AI, Porspoder).
 864 (b) Porphyritic monzogranite exhibiting red orthoclase megacrysts (W-AI, Porspoder). (c)
 865 Mingling pattern between quartz-monzodiorite and two-mica leucogranite (NO, site OS1, Fig.
 866 1c). (d) Dyke of leucominette (W-AI, Porspoder). (e) 1.50 m-thick dyke of alkali-feldspar
 867 quartz microsyenite (NO, site OS11, Fig. 1c). (f) Photomicrograph of the tourmaline-
 868 leucogranite AI2 (Afs: alkali feldspar; Gt: garnet; Tm: tourmaline; Qz: quartz). (g)
 869 Photomicrograph of the leucominette AI33 (Bi: biotite).

870
 871 Fig. 6. Discrimination diagrams for biotite in peraluminous granitoids (Abdel-Rahman, 1994)
 872 and for biotite and phlogopite in lamprophyres (Rock, 1987). AL: alkaline lamprophyres;
 873 CAL: calc-alkalic lamprophyres ; UML: ultramafic lamprophyres; LL : lamproites.

874
 875 Fig. 7. Discrimination diagrams based on major elements for the AI-NO granitoids,
 876 metasedimentary xenoliths and ultrapotassic dykes. (a) Plot of $\text{FeO}^*/(\text{FeO}^* + \text{MgO})$ vs. SiO_2 ,
 877 showing the limit between ferroan and magnesian granitoids (Frost et al., 2001). (b) Plot of
 878 $\text{Na}_2\text{O} + \text{K}_2\text{O} - \text{CaO}$ (modified alkali-lime index, MALI) vs. SiO_2 , showing the approximate
 879 ranges for the alkali, alkali-calcic, calc-alkalic, and calcic rock series (Frost et al., 2001). (c)
 880 Plot of ASI (aluminium saturation index) vs. SiO_2 , showing the limit between metaluminous
 881 and peraluminous granitoids (solid straight line) and the limit between moderately and
 882 strongly peraluminous granitoids (dashed line) (Sylvester, 1998; Frost et al., 2001). (d) K_2O

883 vs. SiO₂ diagram of Peccerillo and Taylor (1976), showing also the calc-alkalic lamprophyre
884 field of Rock (1987). Symbols as in Figs. 2 and 3.

885

886 Fig. 8. Variation of MgO, Al₂O₃, P₂O₅, Ba, Eu, and Y vs. SiO₂ for the AI-NO granitoids,
887 metasedimentary xenoliths and ultrapotassic dykes. The dashed line connects the porphyritic
888 syenogranite AI7, the Afs quartz microsyenite OS11 and the leucominette 13DB07 (see text
889 for explanations). Symbols as in Figs. 2, 3, and 7.

890

891 Fig. 9. CI-chondrite normalized trace element patterns of AI-ON rocks (normalization values:
892 Barrat et al., 2012). (a) Moderately peraluminous (MP) granitoids and strongly peraluminous
893 (SP) syenogranites. (b) SP leucogranites, metasedimentary xenoliths and ultrapotassic dykes.
894 Numbers indicate the four sectors appearing in the patterns of the tourmaline-leucogranites
895 AI2 and AI3a, reflecting a tetrad effect (see text).

896

897 Fig. 10. (a) ϵ_{Nd}^t vs. initial $^{87}\text{Sr}/^{86}\text{Sr}$ isotope diagram showing selected AI-NO data compared
898 with pelites and late-Variscan peraluminous granites from the Spanish Central Region (SCR)
899 (Villaseca et al., 1998). Symbols as in Figs. 2, 3 and 7. (b) ϵ_{Nd}^t vs. initial $^{87}\text{Sr}/^{86}\text{Sr}$ isotope
900 diagram showing the fields of meta-sedimentary middle-upper crust and lower crust (data
901 from the French Massif Central: Downes and Duthou, 1988; Turpin et al., 1990). Note that
902 the lower crustal metasediments have lower initial $^{87}\text{Sr}/^{86}\text{Sr}$ and higher initial ϵ_{Nd} than the
903 middle-upper ones, probably due to isotopic disequilibrium during deep melting of crustal
904 material (Barbero et al., 1995). Such a model might also explain the isotopic difference
905 between the hornfels AI27 and the migmatite AI11 (Fig. 10a).

906

907 Fig. 11. Block diagram showing magma emplacement via the PGSZ/NOSZ in the W-AI and
 908 NO sectors. Colors as in Fig. 1.

909

910 Fig. 12. Plot of (a) K/Ba and (b) Eu/Eu* vs. $TE_{1,3}$ for the AI-NO rocks (except quartz
 911 monzodiorites, granodiorites, metasedimentary xenoliths and ultrapotassic dykes). The
 912 parameter $TE_{1,3}$ of Irber (1999), used to quantify the degree of tetrad effect, is developed in
 913 Table 1. The common range of continental rocks is from Jahn et al. (2001). Symbols as in Fig.
 914 2.

915

916 Fig. 13. Compositions of the AI-NO rocks compared to the fields of two peraluminous granite
 917 types and metapelites (field contours drawn according to the data of Patiño Douce, 1999). The
 918 solid lines correspond to reaction curves that model melt compositions resulting from
 919 hybridization of high-Al olivine tholeiite with metapelite (Patiño Douce, 1995, 1999). LP:
 920 low pressure ($P \leq 0.5$ GPa); HP: high pressure ($1.2 \leq P \leq 1.5$ GPa).

921

922 Fig. 14. Geochemical diagrams for post-collisional SP granites, inspired from Sylvester
 923 (1998). Symbols as in Figs. 2, 3, and 7. (a) Plot of CaO/Na_2O vs. Al_2O_3/TiO_2 for the AI-NO
 924 SP granites, metasedimentary xenoliths and ultrapotassic dykes. The MP data are shown as a
 925 field, together with the Sylvester's (1998) SP granites. The solid line correspond to the mixing
 926 curve (percentage of mixing indicated) between the average Phanerozoic basalt of Condie
 927 (1993) and the 850°C, 1 GPa pelite-derived melt of Patiño Douce and Johnston (1991). (b)
 928 Plot of Rb/Ba vs. Rb/Sr for the same samples. The dashed line divides the SP granite field
 929 according to the clay content of the source. The Condie's (1993) average Phanerozoic basalt
 930 and calculated composition of pelite- and psammite-derived SP granitic melts are also
 931 indicated, together with a calculated basalt/pelite-derived melt mixing curve (percentage of

932 mixing marked) (Sylvester, 1998). Note that the AI leucominettes plot very close to the
933 average basalt.

934

935 Fig. 15. Conceptual model for the genesis of post-collisional MP and SP granitoids in a
936 thinned and hot lithosphere in the Variscides. Not to scale. Modified after Sylvester (1998).

937

Table 1. Major and trace element data on whole rock.

Type:	Q-MD / GD			P-MG					P-SG	2M-SG			2M-LG	
Location:	W-AI	W-AI	NO	W-AI	W-AI	E-AI	NO	NO	W-AI	W-AI	W-AI	Off.sh.	W-AI	
Sample:	AI6b	AI28	OS1	AI26	13DB05	AI31	LC3	LC4	AI7	AI17	AI23	C34	AI5	
<i>Major elements (wt.%)</i>														
SiO ₂	65.04	58.60	59.30	64.55	67.30	69.90	71.75	70.10	71.10	72.28	73.40	73.70	73.40	
TiO ₂	0.99	1.50	1.45	0.78	0.70	0.52	0.34	0.37	0.30	0.20	0.34	0.28	0.23	
Al ₂ O ₃	15.38	17.00	16.60	15.22	16.20	15.40	14.02	14.52	14.90	13.76	14.80	14.10	13.50	
Fe ₂ O ₃ ^{tot}	6.11	7.80	6.80	4.79	4.30	3.40	2.10	2.52	2.30	1.64	2.40	2.20	1.49	
MnO	0.12	0.10	0.09	0.06	0.07	0.07	0.05	0.53	0.05	0.05	0.03	0.05	0.03	
MgO	1.68	2.81	3.68	1.38	1.30	1.00	0.65	0.76	0.58	0.30	0.62	0.54	0.34	
CaO	2.37	4.37	3.83	2.72	2.62	2.10	0.83	1.03	1.07	0.85	1.29	0.70	0.75	
Na ₂ O	3.90	3.74	3.23	3.17	3.22	3.58	4.00	4.09	3.19	3.24	2.74	3.03	2.62	
K ₂ O	2.45	2.84	3.48	4.66	4.55	4.19	4.63	4.55	5.50	4.53	5.17	4.69	5.90	
P ₂ O ₅	0.36	0.62	0.42	0.30	0.26	0.17	0.17	0.19	0.17	0.22	0.15	0.25	0.24	
LOI	1.32	0.75	1.16	0.50	0.76	0.74	1.10	1.14	0.74	0.98	0.88	1.24	0.73	
Total	99.72	100.13	100.04	98.12	101.28	101.08	99.64	99.80	99.90	98.04	101.81	100.78	99.24	
ASI	1.19	1.03	1.07	1.03	1.10	1.10	1.09	1.09	1.15	1.20	1.21	1.28	1.15	
<i>Trace elements (ppm)</i>														
Li	504	167	265	122	131	126	-	-	137	376	81.7	185	122	
Be	7.0	6.4	6.3	6.1	6.9	9.1	-	-	5.4	15.2	9.3	14.2	14.0	
Rb	273	229	280	210	229	222	-	-	276	307	207	359	252	
Cs	19.9	16.1	40.5	10.9	19.4	16.6	-	-	16.1	30.4	11.6	22.1	13.5	
Sr	175	356	439	335	316	283	-	-	163	117	162	137	84	
Ba	196	407	586	802	715	521	-	-	457	222	426	242	232	
Sc	10	13	14	9	9	6	-	-	6	4	5	5	2	
V	76.6	119	120	60.9	51.5	38.1	-	-	18.6	10.4	18.3	15.9	9.4	
Cr	9	27	67	33	11	25	-	-	19	10	31	13	9	
Co	11.3	18.3	24.2	10.1	9.8	6.2	-	-	3.1	2.0	3.6	1.8	1.4	
Ni	7.6	19.8	49.4	7.6	8.6	6.2	-	-	3.6	1.5	3.2	1.9	1.6	
Cu	1.9	11.7	8.8	7.2	4.5	0.7	-	-	0.5	0.4	8.2	0.5	0.4	
Zn	110	128	135	80	76	122	-	-	58	39	47	42	42	
Y	24	29	22	21	21	18	-	-	19	13	12	12	10	
Zr	212	225	201	144	286	114	-	-	131	69	86	72	90	
Hf	5.3	4.5	5.3	3.8	7.1	3.4	-	-	3.9	2.3	2.8	3.2	2.8	
Nb	26	34	31	22	21	21	-	-	22	17	11	21	10	
Ta	2.0	1.9	2.0	1.4	1.4	1.9	-	-	2.0	3.0	0.8	3.6	1.3	
W	10.3	6.8	6.0	9.8	10.8	5.1	-	-	15.2	29.3	18.1	52.0	15.6	
Ga	23	23	24	22	24	23	-	-	22	22	20	24	20	
Pb	16.8	12.1	11.3	23.8	20.4	21.5	-	-	33.3	34.4	33.5	29.8	30.7	
La	68.2	89.4	46.0	67.7	76.8	67.8	-	-	57.8	24.4	34.8	24.8	23.4	
Ce	132	173	90.7	137	142	133	-	-	112	47.1	72.5	52.3	51.2	
Pr	14.1	18.8	11.6	14.8	14.8	13.3	-	-	11.8	5.3	8.4	6.3	6.1	
Nd	50.1	71.2	43.3	54.0	53.1	44.6	-	-	40.4	18.4	30.0	26.8	21.7	
Sm	8.5	11.8	8.0	8.8	8.7	6.8	-	-	7.0	3.6	6.2	5.3	5.3	
Eu	1.05	1.86	1.82	1.71	1.55	1.26	-	-	0.96	0.56	1.06	0.70	0.50	
Gd	6.48	9.09	6.68	6.40	6.51	5.12	-	-	5.35	3.12	4.45	3.60	4.38	
Tb	0.89	1.15	0.87	0.82	0.85	0.65	-	-	0.73	0.48	0.58	0.53	0.57	
Dy	4.64	5.56	4.41	4.00	4.17	3.31	-	-	3.68	2.57	2.65	2.85	2.50	
Ho	0.87	0.99	0.81	0.76	0.77	0.61	-	-	0.67	0.46	0.42	0.51	0.37	
Er	2.31	2.58	2.11	1.94	2.07	1.68	-	-	1.72	1.21	0.96	1.44	0.86	
Yb	2.04	1.98	1.69	1.59	1.69	1.49	-	-	1.51	1.14	0.71	1.38	0.64	
Lu	0.27	0.27	0.23	0.23	0.23	0.21	-	-	0.21	0.15	0.09	0.19	0.08	
Th	20.0	14.8	15.3	22.2	20.4	36.6	-	-	25.9	12.4	21.0	15.8	15.8	
U	5.4	6.8	8.7	6.9	3.8	12.9	-	-	7.1	5.3	5.9	2.1	5.2	
TE _{1,3}	0.99	0.97	0.98	0.98	0.97	1.00	-	-	1.01	1.04	1.04	1.00	1.07	

Table 1. (continued)

Type:	2M-LG			T-LG		μ G	μ SY	CAL			MIG	HF
Location:	W-AI	E-AI	NO	W-AI	W-AI	W-AI	NO	W-AI	W-AI	W-AI	W-AI	W-AI
Sample:	AI19	AI30	OS4	AI2	AI3a	AI32	OS11	AI33	13DB06	13DB07	AI11	AI27
<i>Major elements (wt.%)</i>												
SiO ₂	74.20	73.90	74.07	74.77	76.97	74.96	63.10	55.50	57.30	56.90	65.58	60.10
TiO ₂	0.14	0.15	0.15	0.05	0.06	0.12	0.73	1.46	1.37	1.50	0.75	0.89
Al ₂ O ₃	15.00	14.90	13.34	13.19	12.37	13.61	15.30	15.20	15.00	15.30	13.97	17.10
Fe ₂ O ₃ ^{tot}	1.20	1.30	1.32	0.76	0.54	1.06	4.60	6.80	6.70	6.70	6.65	5.80
MnO	0.03	0.03	0.03	0.12	0.02	0.02	0.04	0.08	0.08	0.07	0.15	0.11
MgO	0.29	0.29	0.22	0.03	0.08	0.18	2.26	3.77	3.72	3.82	1.98	1.80
CaO	0.64	0.63	0.45	0.22	0.25	0.37	1.00	5.42	2.7	2.80	0.62	1.41
Na ₂ O	3.32	3.41	3.11	3.76	3.08	3.06	2.44	2.08	2.58	2.53	2.22	2.35
K ₂ O	4.91	4.84	4.79	3.96	4.24	4.97	6.65	5.33	6.30	6.30	5.13	8.26
P ₂ O ₅	0.32	0.28	0.37	0.23	0.15	0.33	0.75	1.36	1.31	1.34	0.10	0.20
LOI	1.00	0.99	1.21	1.10	0.85	1.25	2.38	1.94	1.53	1.55	1.41	0.75
Total	101.04	100.72	99.05	98.19	98.61	99.93	99.24	98.94	98.59	98.81	98.56	98.76
ASI	1.30	1.28	1.25	1.25	1.25	1.27	1.26	0.87	1.04	1.06	1.37	1.13
<i>Trace elements (ppm)</i>												
Li	184	194	59.3	93.9	82.8	76.8	169	180	145	147	487	140
Be	7.5	7.9	7.7	2.4	3.9	3.1	12.2	4.4	6.1	6.4	10.7	4.2
Rb	239	291	279	453	345	316	309	223	186	185	416	331
Cs	23.1	19.8	18.3	14.4	17.4	11.4	6.94	20.2	7.66	7.85	36.5	25.6
Sr	79	77	60	11	33	52	327	2500	2490	2430	74	169
Ba	186	184	156	13	42	136	2380	5310	5690	5620	407	521
Sc	4	3	4	8	2	3	11	15	16	17	13	14
V	6.4	6.0	4.1	0.3	2.6	3.4	82.0	122	128	127	104	115
Cr	5	8	14	2	3	13	48	84	85	80	83	81
Co	1.0	1.4	0.7	0.3	0.6	0.6	11.7	19.4	19.2	11.3	10.6	16.3
Ni	1.1	1.2	0.3	0.3	0.1	0.4	30.5	57.9	60.0	51.6	32.4	34.8
Cu	0.9	0.5	3.5	1.0	0.3	2.9	52.3	7.6	6.5	7.0	1.7	35.3
Zn	43	73	50	28	14	49	127	108	144	142	140	101
Y	12	13	12	4	5	10	23	39	48	50	12	29
Zr	51	66	49	17	17	51	286	566	732	727	70	93
Hf	1.8	2.2	2.0	1.3	0.9	2.0	7.0	12.0	13.8	13.8	1.9	2.6
Nb	12	16	16	29	6	16	15	29	36	37	20	20
Ta	1.9	2.2	2.7	4.7	2.5	2.3	0.8	1.3	1.7	1.7	1.8	1.5
W	19.8	22.5	49.2	62.4	25.5	37.3	58.7	19.1	4.8	5.6	21.0	12.2
Ga	20	23	22	35	21	22	21	21	22	22	22	22
Pb	32.5	31.2	30.6	15.7	21.1	22.7	24.2	20.1	37.2	38.3	22.8	40.1
La	10.9	15.0	10.9	2.1	5.5	9.8	60.8	205	237	291	28.4	43.7
Ce	24.0	34.2	23.6	4.2	11.0	21.8	128.9	399	468	543	57.9	99.0
Pr	2.8	3.9	3.0	0.5	1.3	2.7	14.3	47.8	53.2	60.7	6.6	10.8
Nd	10.3	13.9	11.4	1.8	4.1	11.7	55.5	176	194	222	24.2	40.0
Sm	2.5	3.3	2.8	0.7	1.0	3.0	10.4	26.2	28.6	31.1	4.7	8.2
Eu	0.38	0.40	0.31	0.02	0.10	0.32	2.33	6.43	6.47	6.64	0.62	1.40
Gd	2.38	3.02	2.77	0.63	0.91	2.85	7.99	17.56	16.81	17.83	3.88	7.45
Tb	0.43	0.51	0.48	0.13	0.18	0.46	1.00	1.85	1.91	2.02	0.49	1.04
Dy	2.29	2.67	2.38	0.74	1.01	2.30	4.61	7.56	8.60	9.03	2.50	5.42
Ho	0.41	0.43	0.38	0.12	0.17	0.36	0.82	1.25	1.43	1.50	0.44	0.96
Er	1.06	1.03	0.92	0.36	0.47	0.91	2.04	3.04	3.48	3.62	1.11	2.49
Yb	0.91	0.89	0.74	0.55	0.59	0.77	1.67	2.22	2.62	2.74	0.96	2.10
Lu	0.12	0.11	0.09	0.07	0.08	0.10	0.23	0.29	0.36	0.37	0.13	0.28
Th	7.2	9.6	7.5	1.8	2.4	6.6	21.7	29.5	33.6	35.5	9.6	14.0
U	7.9	4.4	4.8	1.0	3.5	12.5	9.3	6.3	6.9	7.3	4.3	2.6
TE _{1,3}	1.11	1.14	1.11	1.17	1.17	1.07	0.99	0.95	0.98	0.96	1.00	1.04

W-(E)-AI: West (East) Aber-Ildut; NO: North-Ouessant. Q-MD: quartz monzodiorite; GD: granodiorite; P-MG: porphyroid monzogranite; P-SG: porphyroid syenogranite; 2M-SG : two-mica syenogranite; 2M-LG : two-mica leucogranite; T-LG : tourmaline-leucogranite; μ G : two-mica microgranite; μ SY : Afs quartz microsyenite; CAL: calc-alkaline lamprophyre (leucominette); MIG: migmatite; HF: hornfels. The aluminum saturation index (ASI) is defined as the molecular ratio Al/(Ca-1.67·P+Na+K) (Frost et al., 2001).

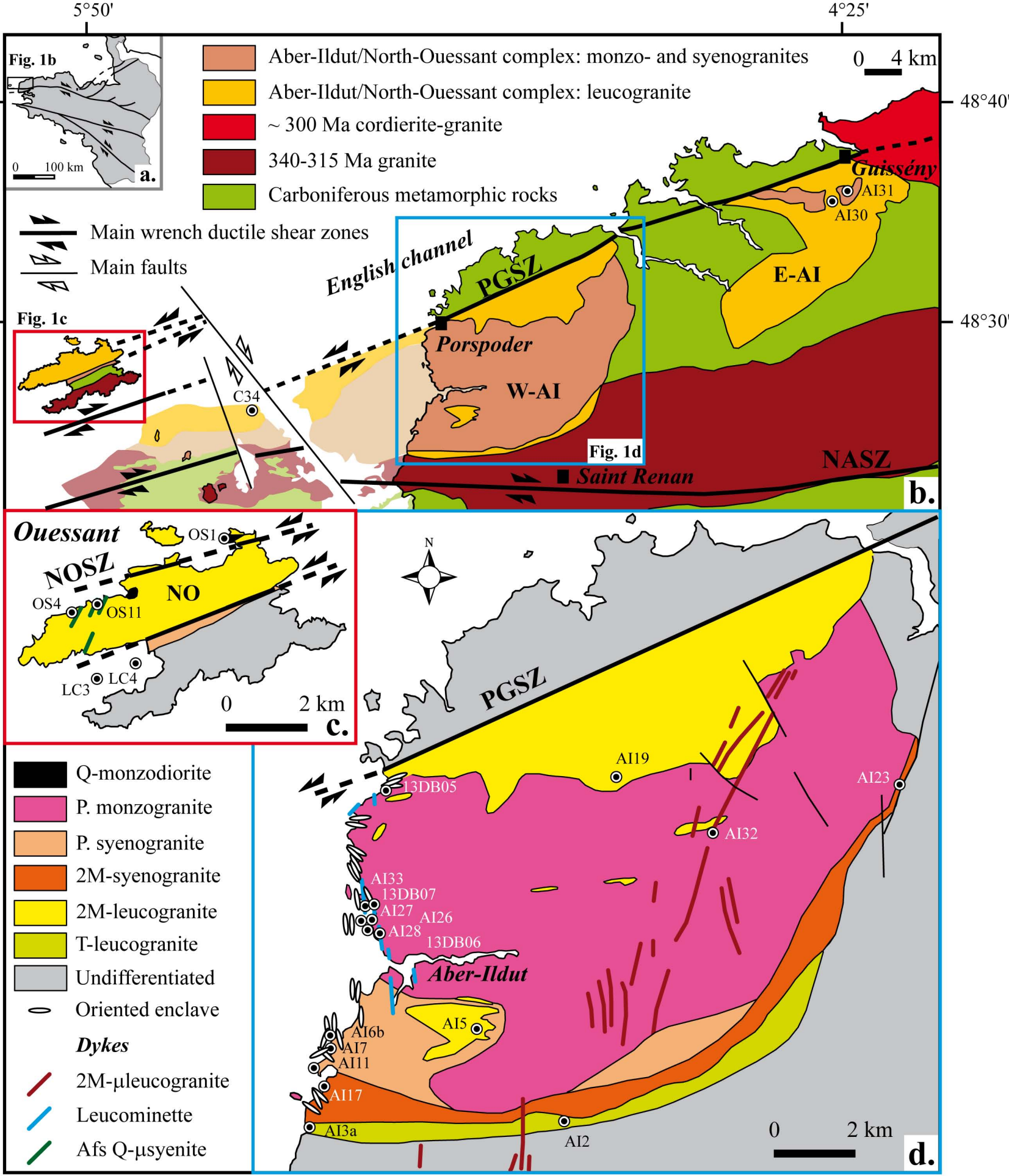
The degree of tetrad effect TE_{1,3} (Irber, 1999) is defined as:

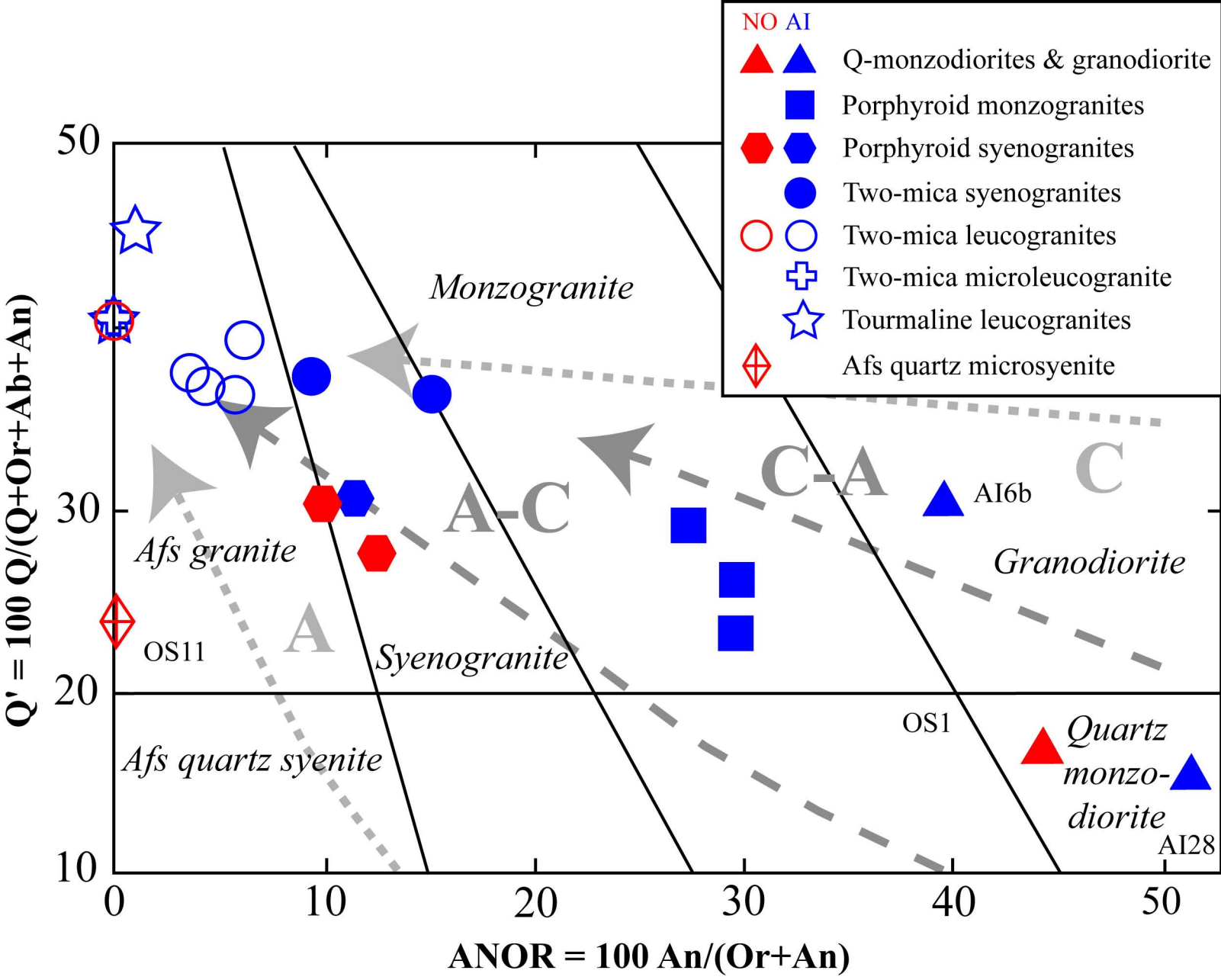
Samples collected during field trips in 2013 and 2014, except LC3 and LC4 (Chauris, 1991) and C34 (Le Gall et al., 2014). Major elements were analyzed by ICP-AES (IUEM, Brest, France) following the analytical method described by Cotten et al. (1995); trace elements were analyzed by ICP-MS (IUEM, Brest, France) following the sample preparation and analysis method of Barrat et al. (1996).

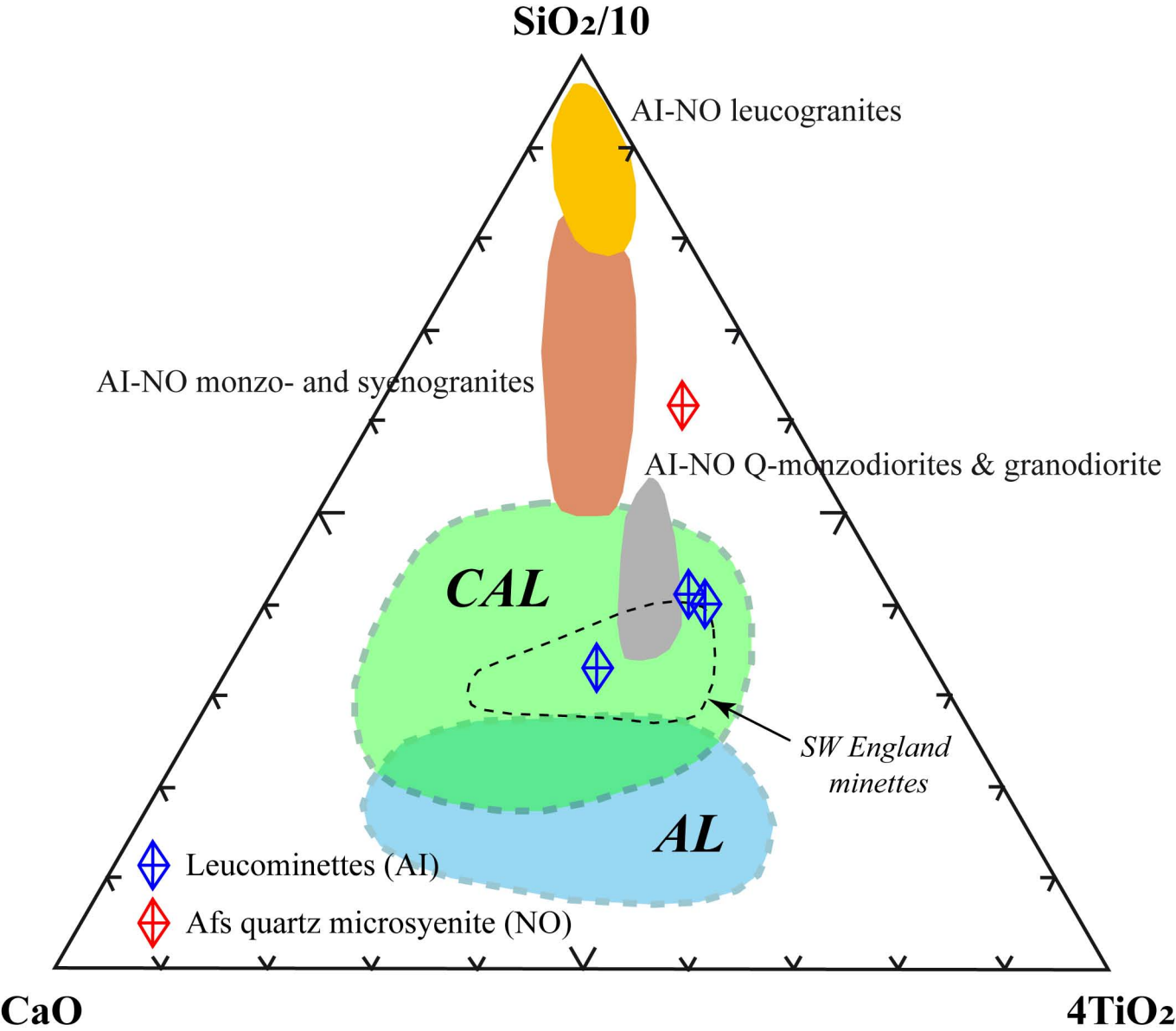
Table 2. Isotopic data on whole rock samples from Aber-Ildut and North-Ouessant.

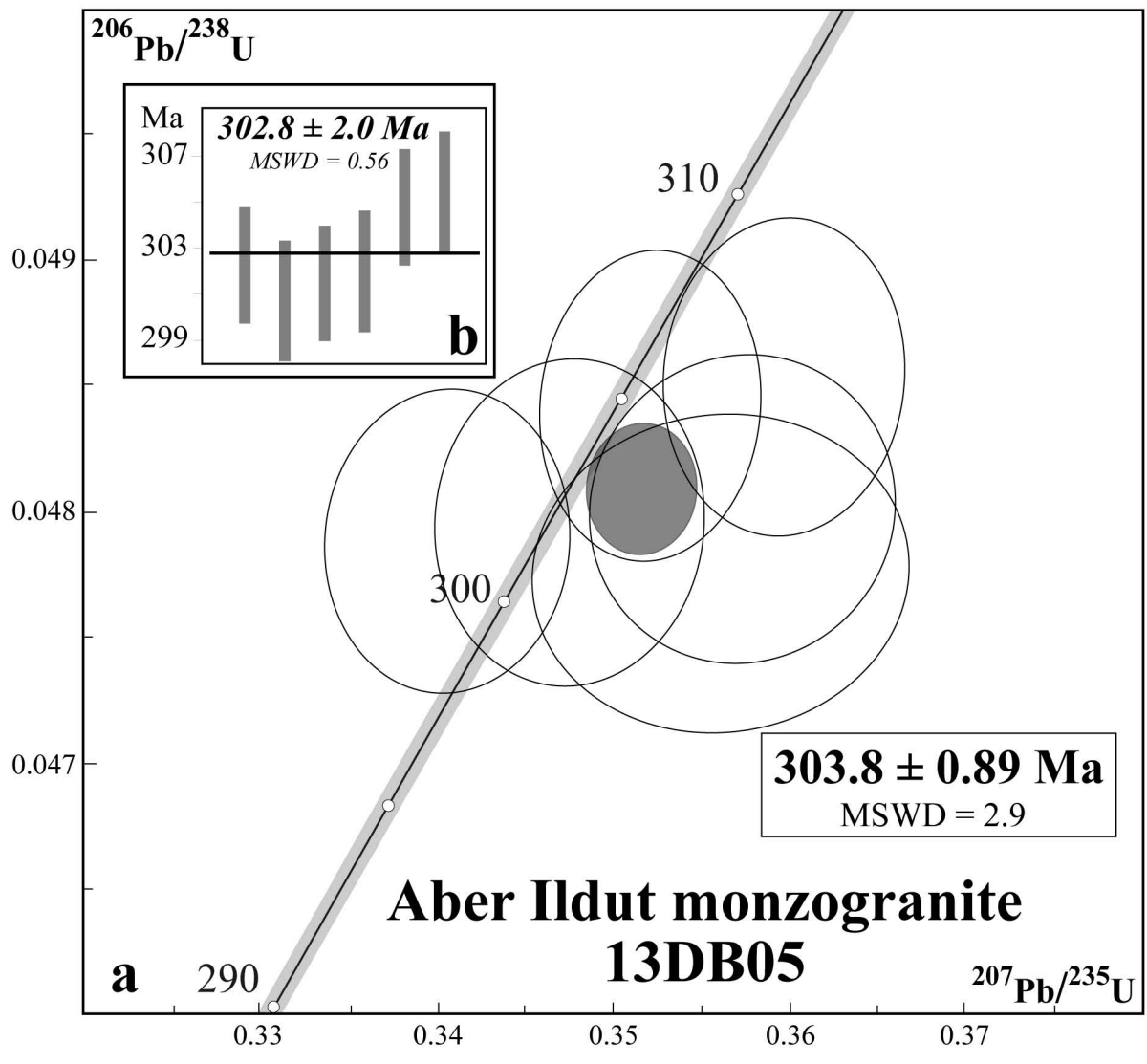
Type	Sample	Rb (ppm)	Sr (ppm)	$^{87}\text{Rb}/^{86}\text{Sr}$	$^{87}\text{Sr}/^{86}\text{Sr}$	$\pm 2\sigma$ ($\times 10^{-6}$)	$(^{87}\text{Sr}/^{86}\text{Sr})_i$	Sm (ppm)	Nd (ppm)	$^{147}\text{Sm}/^{144}\text{Nd}$	$^{143}\text{Nd}/^{144}\text{Nd}$	$\pm 2\sigma$ ($\times 10^{-6}$)	ϵ^t_{Nd}
							($t=304 \text{ Ma}$)						($t=304 \text{ Ma}$)
GD	AI6b	273	175	4.53	0.726221	4	0.70661	8.53	50.1	0.1030	0.512363	4	-1.7
P-MG	AI26	210	335	1.82	0.714056	5	0.70620	8.79	54.0	0.0985	0.512294	4	-2.9
2M-LG	C34	359	137	7.62	0.739488	4	0.70654	5.27	26.8	0.1188	0.512253	6	-4.5
2M-LG	AI19	239	79	8.79	0.750405	4	0.71238	2.46	10.3	0.1447	0.512291	4	-4.7
2M-LG	OS4	279	60	13.53	0.770652	4	0.71211	2.83	11.4	0.1504	0.512273	4	-5.3
T-LG	AI3a	345	33	30.74	0.846528	4	0.71355	1.04	4.1	0.1526	0.512332	7	-4.3
μSY	OS11	309	327	2.74	0.717790	5	0.70592	10.44	55.5	0.1137	0.512325	3	-2.5
CAL	AI33	223	2501	0.26	0.706728	4	0.70561	26.24	176	0.0900	0.512350	3	-2.5
MIG	AI11	416	74	16.44	0.780676	3	0.70957	4.65	24.2	0.1162	0.512212	4	-5.2
HF	AI27	331	169	5.69	0.743674	4	0.71907	8.15	40.0	0.1232	0.511874	4	-12.1

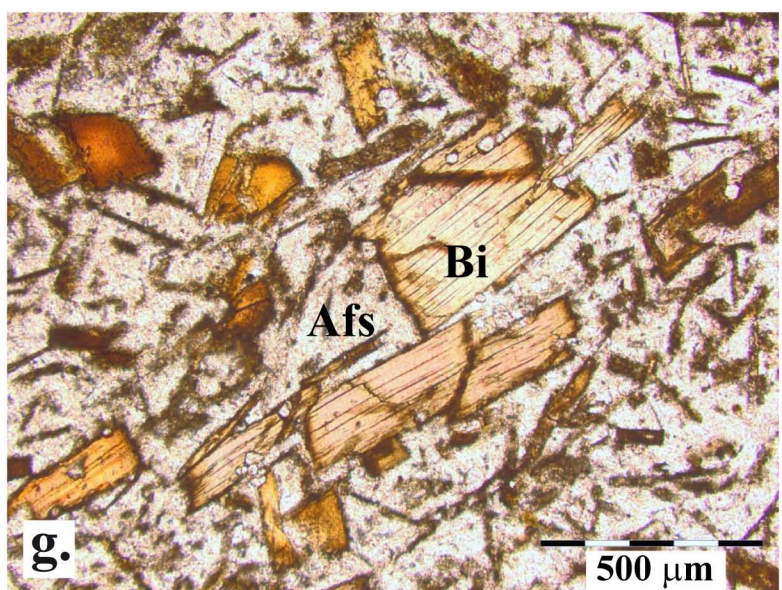
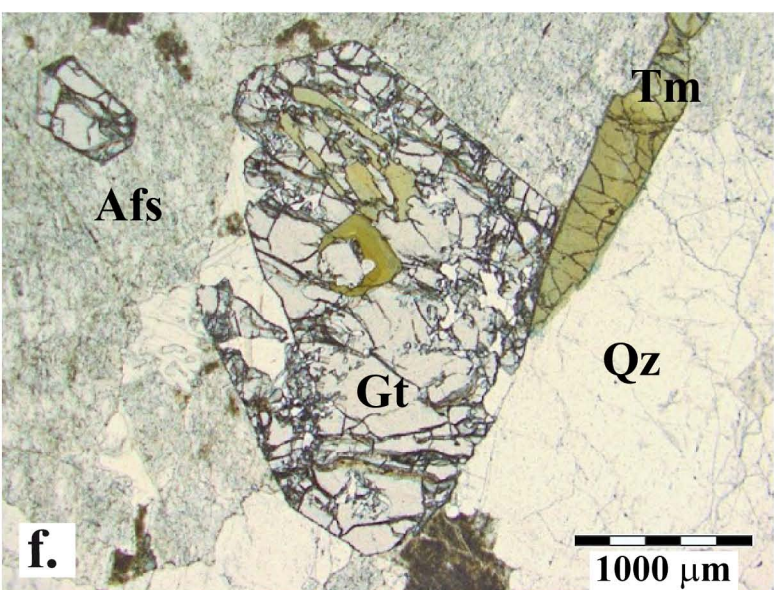
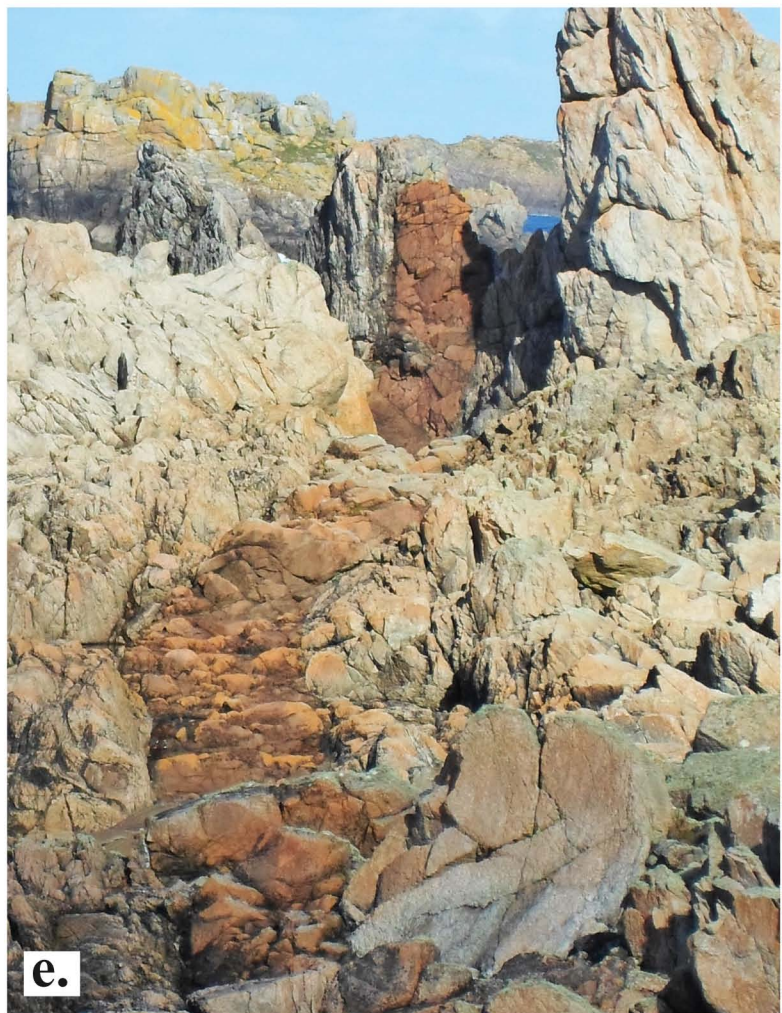
GD: granodiorite; P-MG: porphyritic monzogranite; 2M-LG : two-mica leucogranite; T-LG : tourmaline-leucogranite; μSY : Afs quartz microsyénite; CAL: calc-alkaline lamprophyre (leucominette); MIG: migmatite; HF: hornfels. All Sr and Nd isotope ratios are reported at the 2σ confidence level. The Sr isotopic data were determined by thermal ionization mass spectrometry (TIMS) using a Thermo ElectronTM Triton T1 at the IUEM, Brest, France. Nd isotopic data were determined using a Thermo ElectronTM Neptune MC-ICP-MS at Ifremer, Brest, France. Sr isotopic ratios were normalized to the NBS 987 standard ($^{87}\text{Sr}/^{86}\text{Sr} = 0.710264$) and Nd ratios to JINDI330 standard ($^{143}\text{Nd}/^{144}\text{Nd} = 0.512094$). Measured blanks are 3.9 ppb for Sr and 0.198 ppb for Nd. ϵ^t_{Nd} values have been calculated with the following CHUR values: $^{143}\text{Nd}/^{144}\text{Nd} = 0.512638$ and $^{147}\text{Sm}/^{144}\text{Nd} = 0.1967$. 304 Ma is used as approximate age of crystallization.

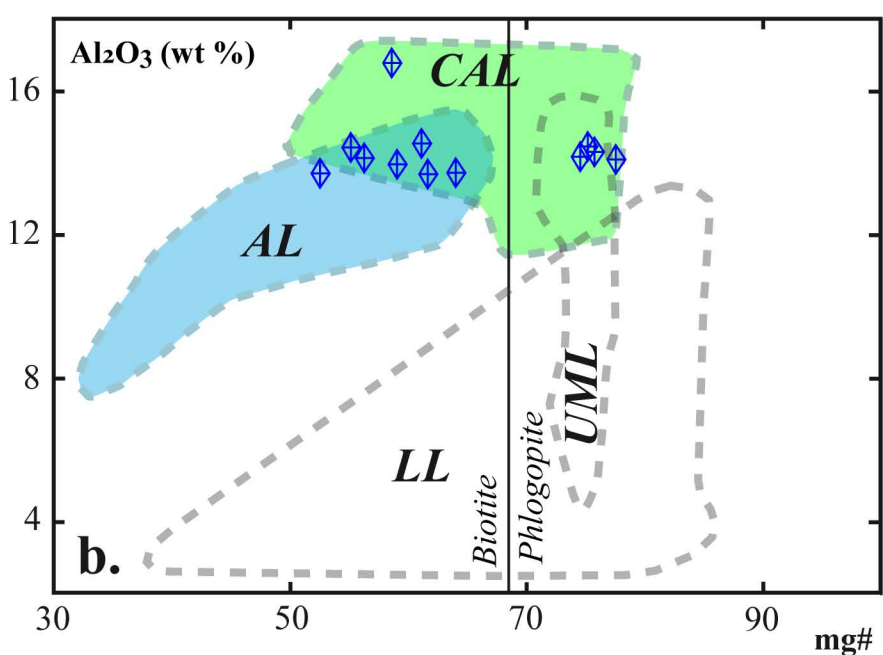
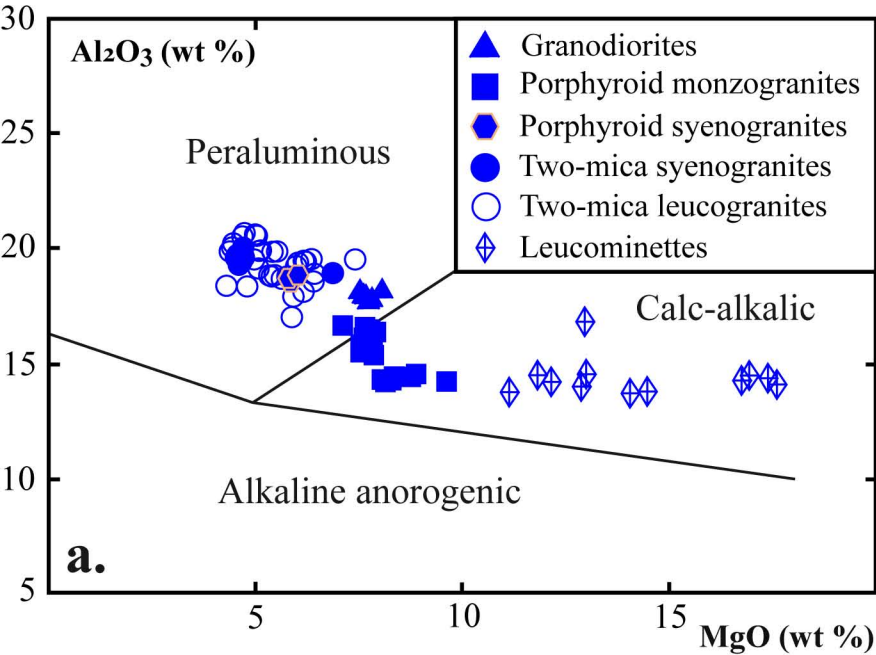


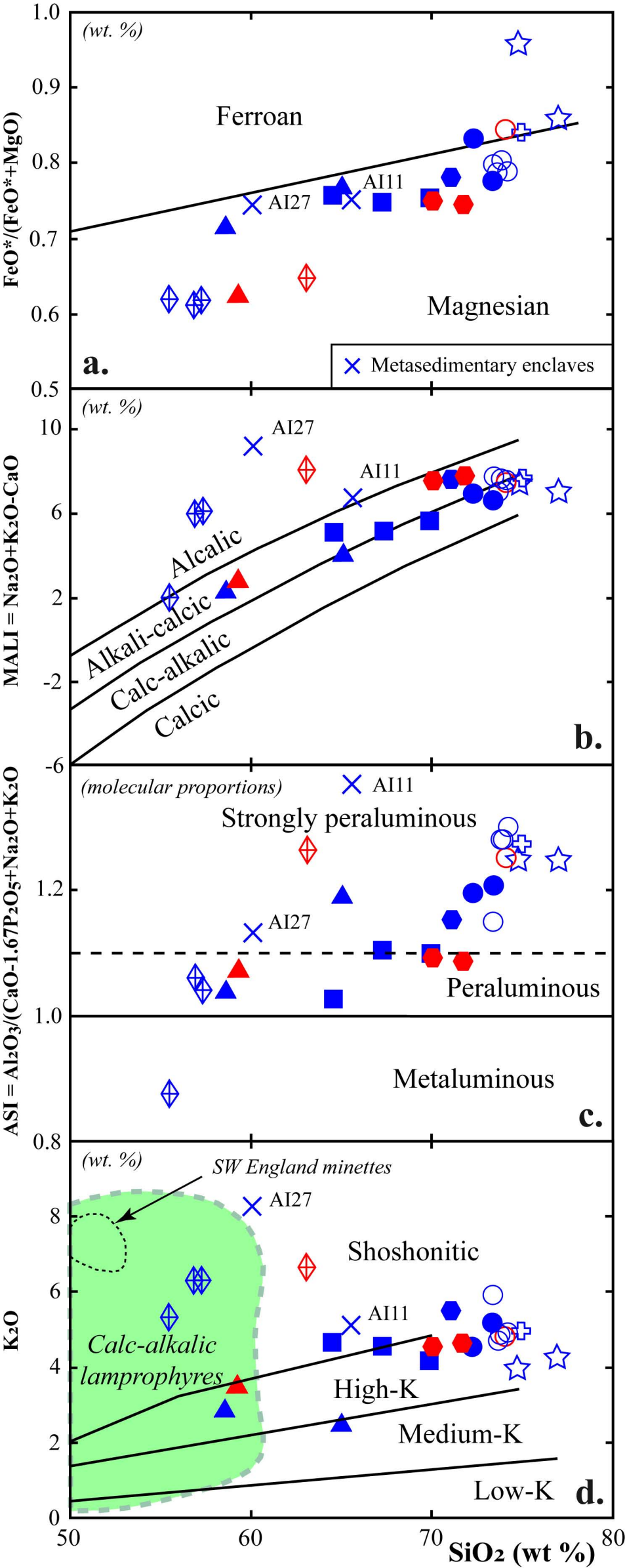


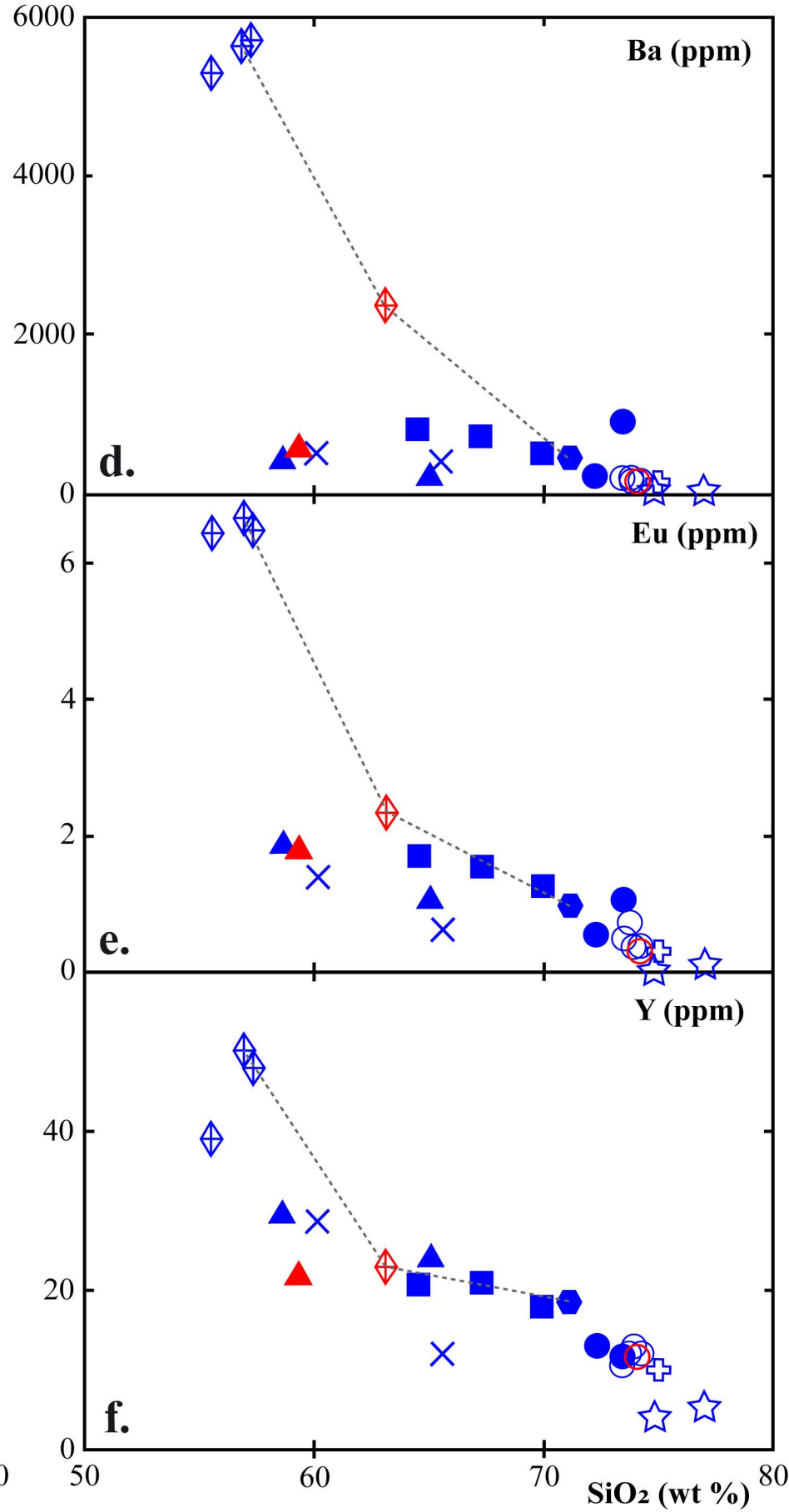
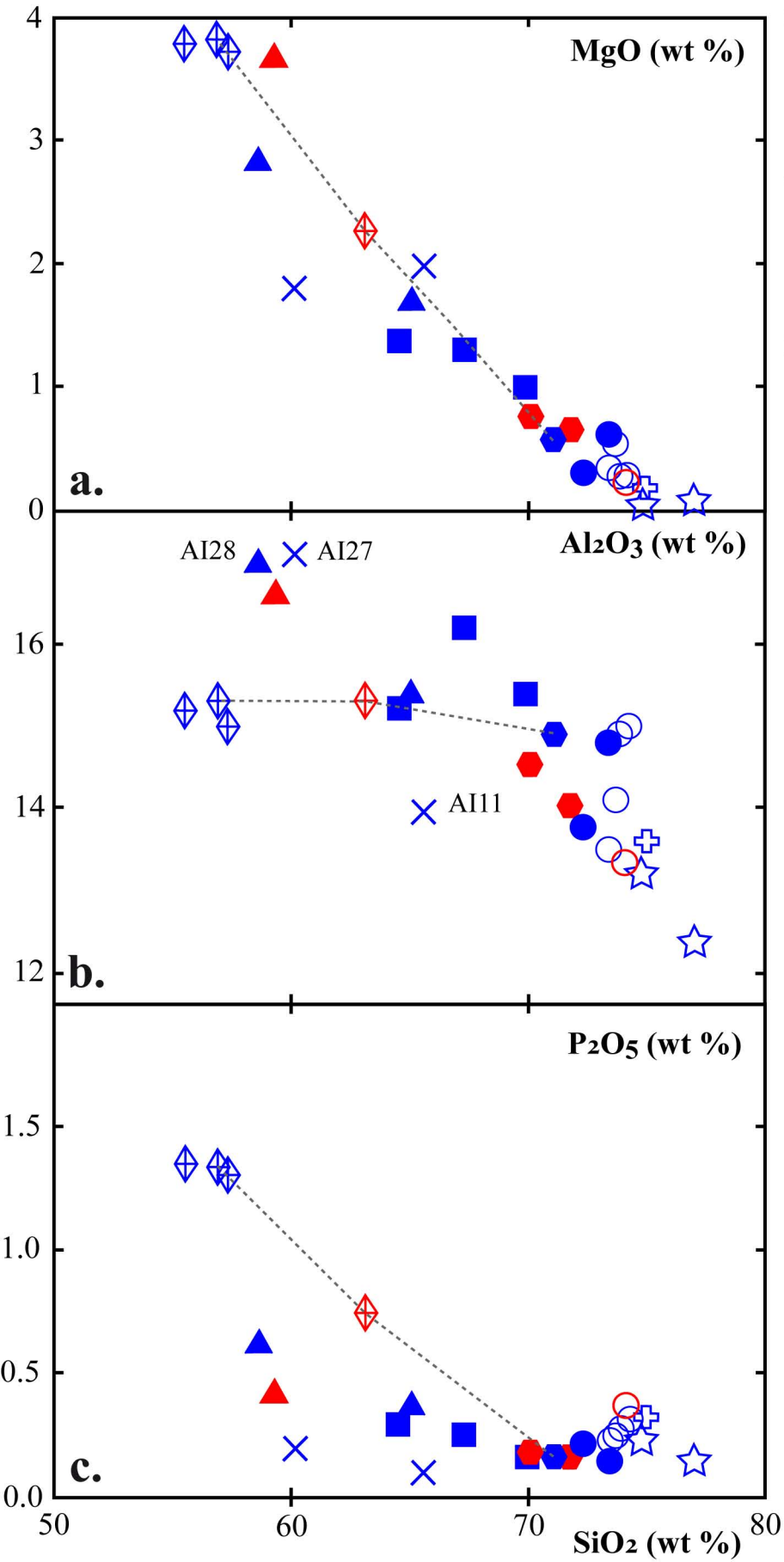


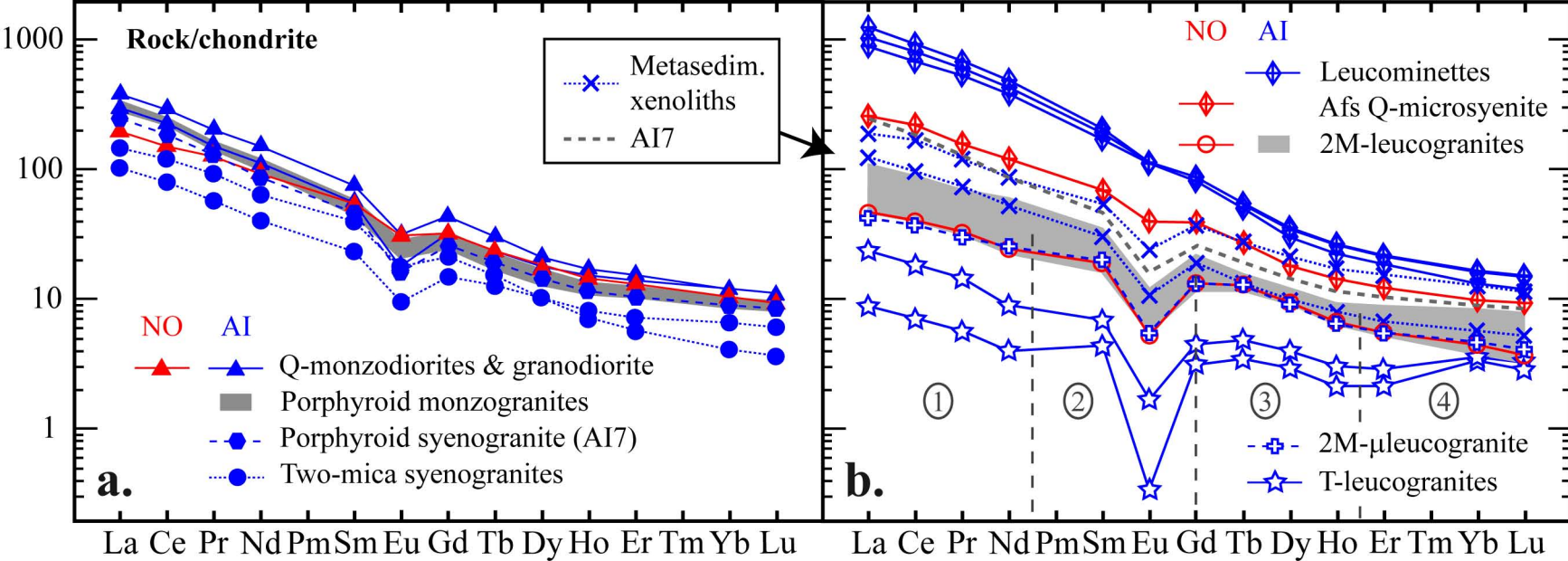


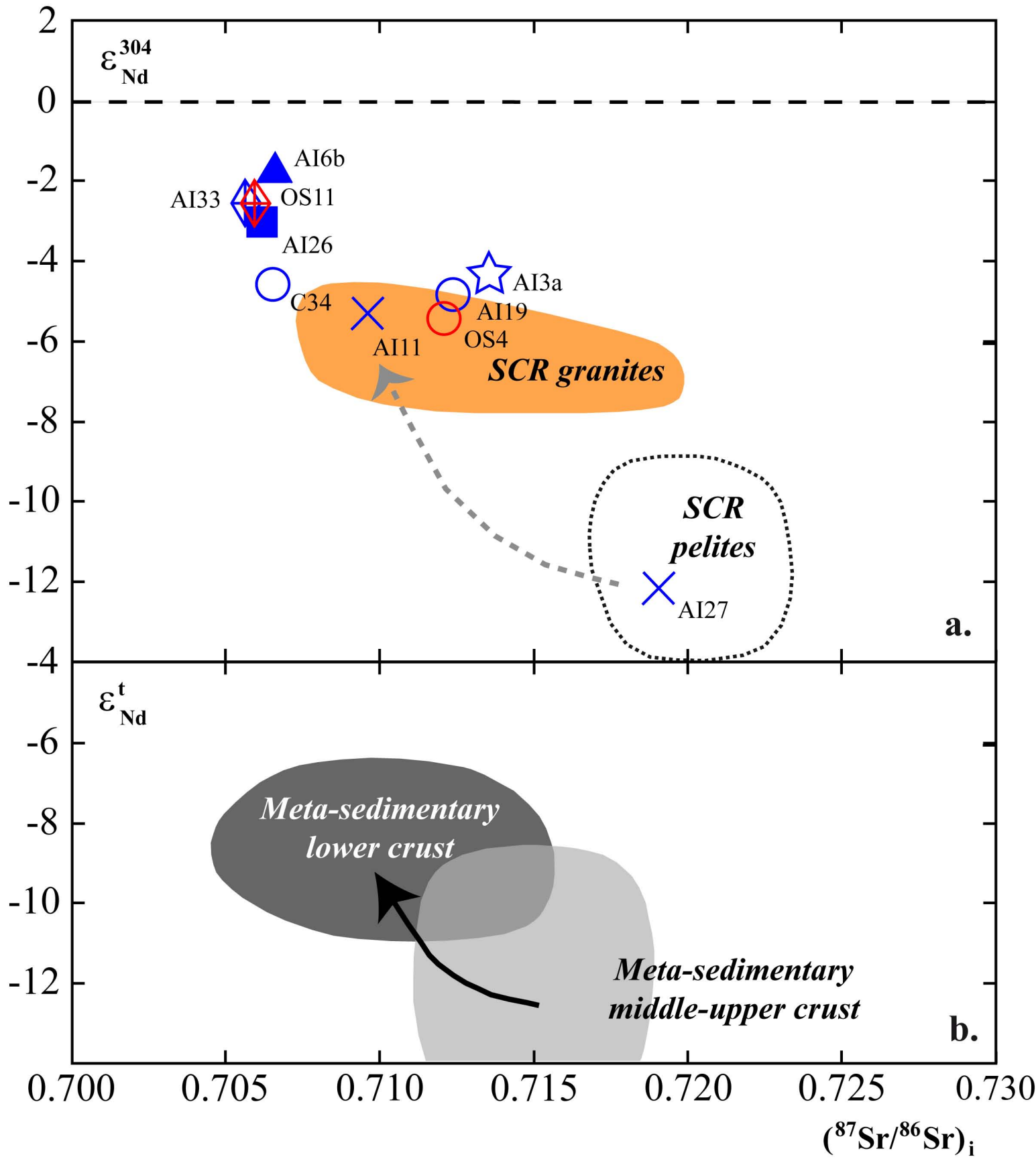


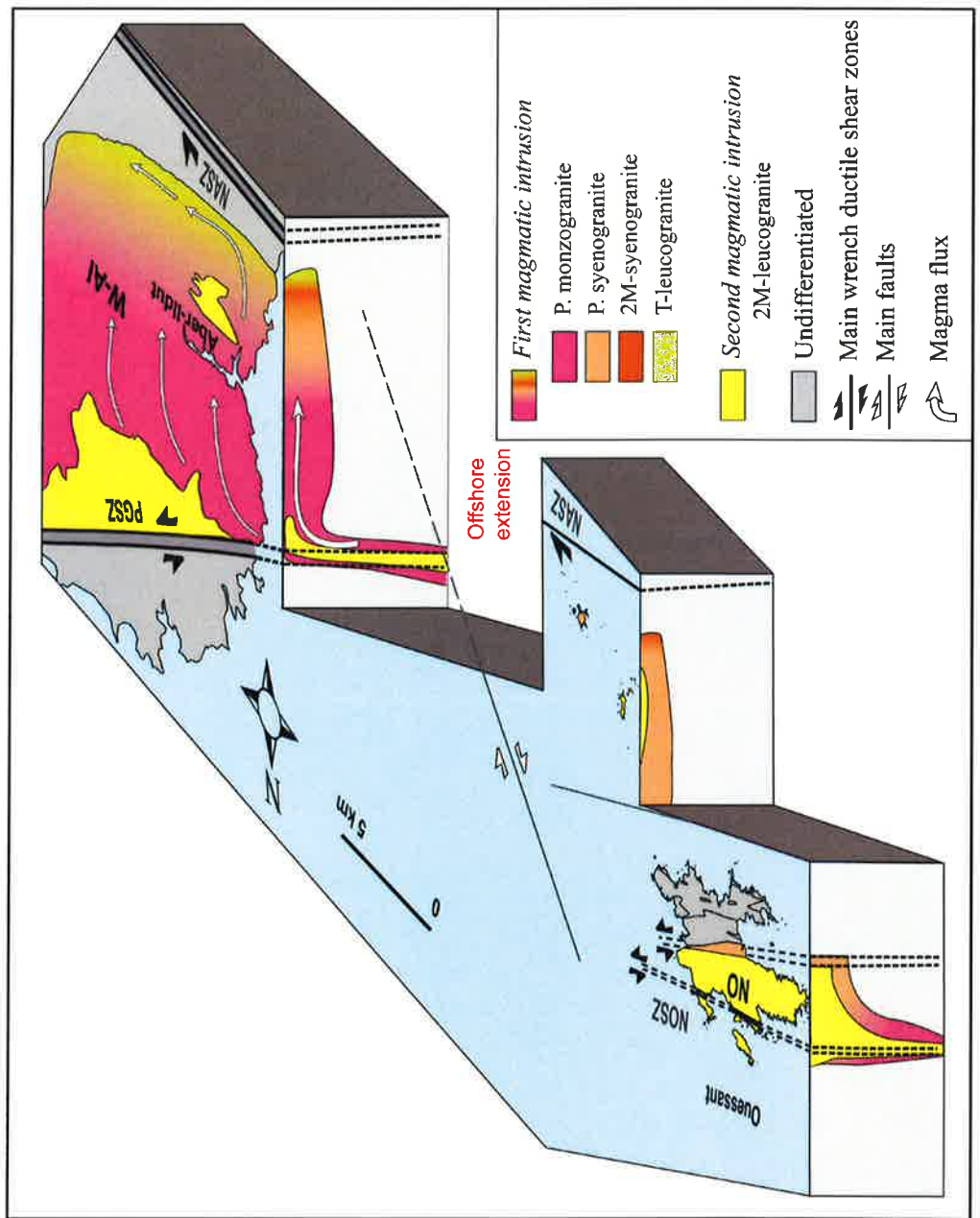


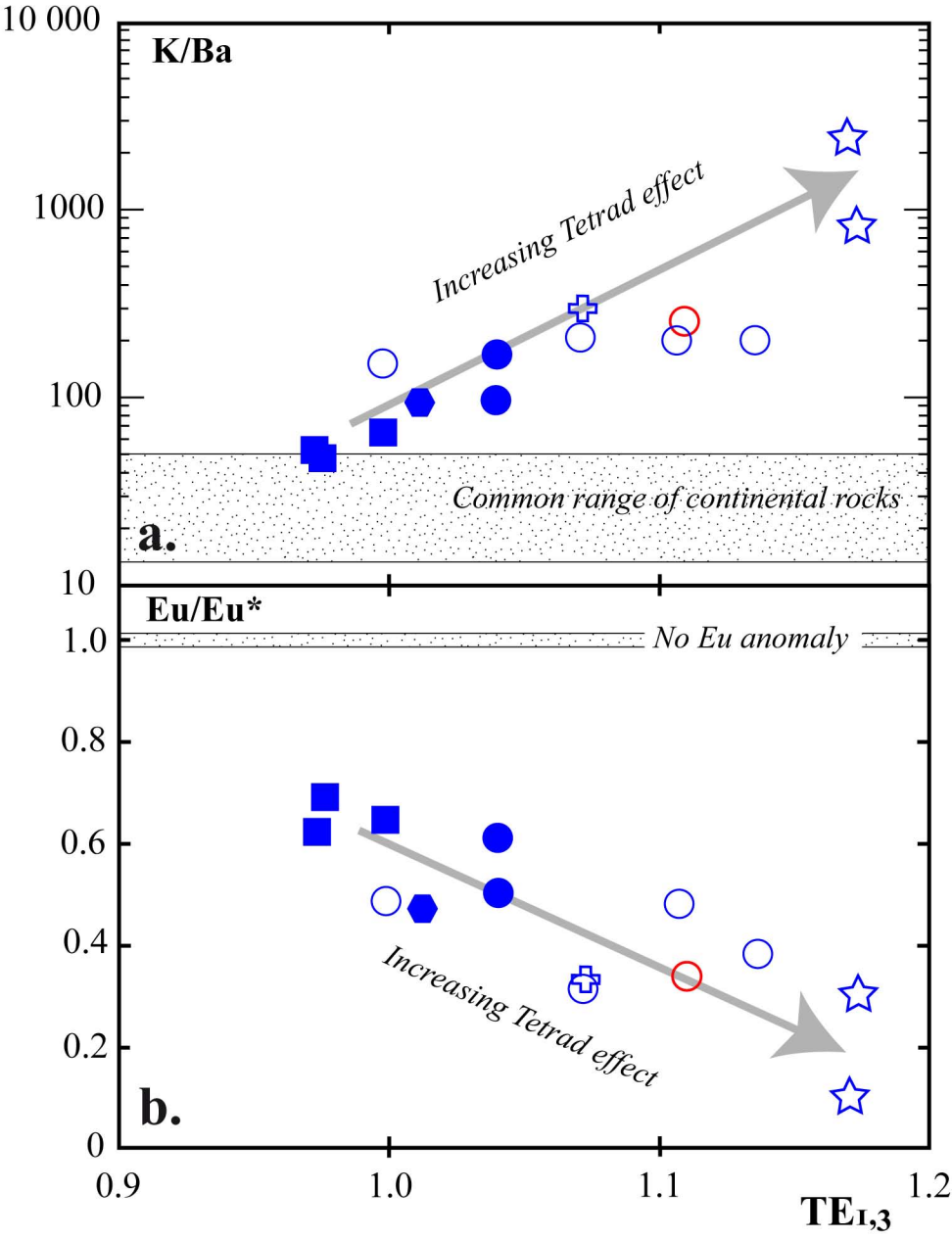


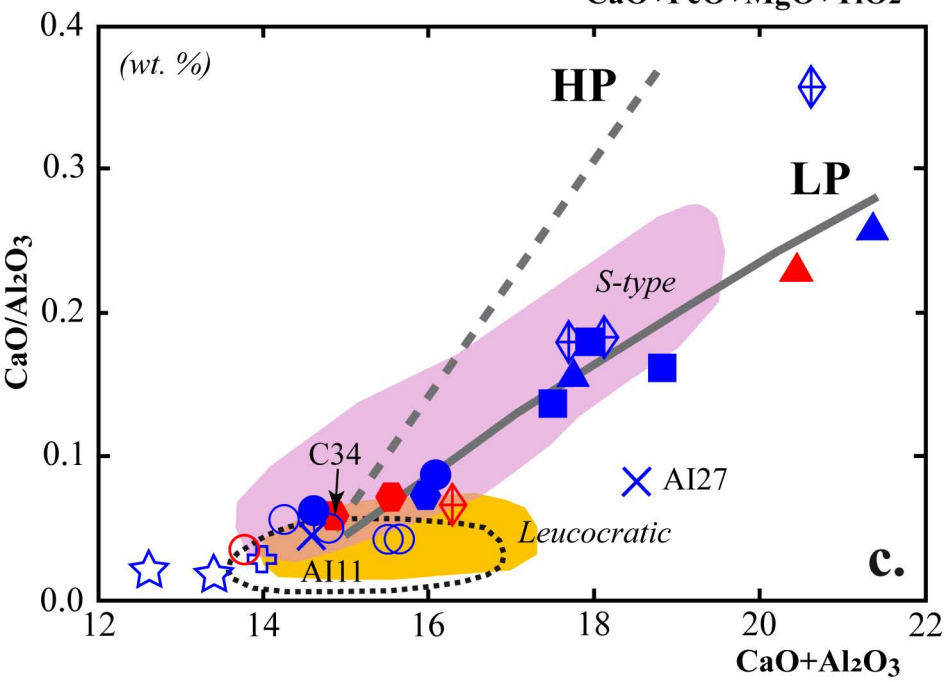
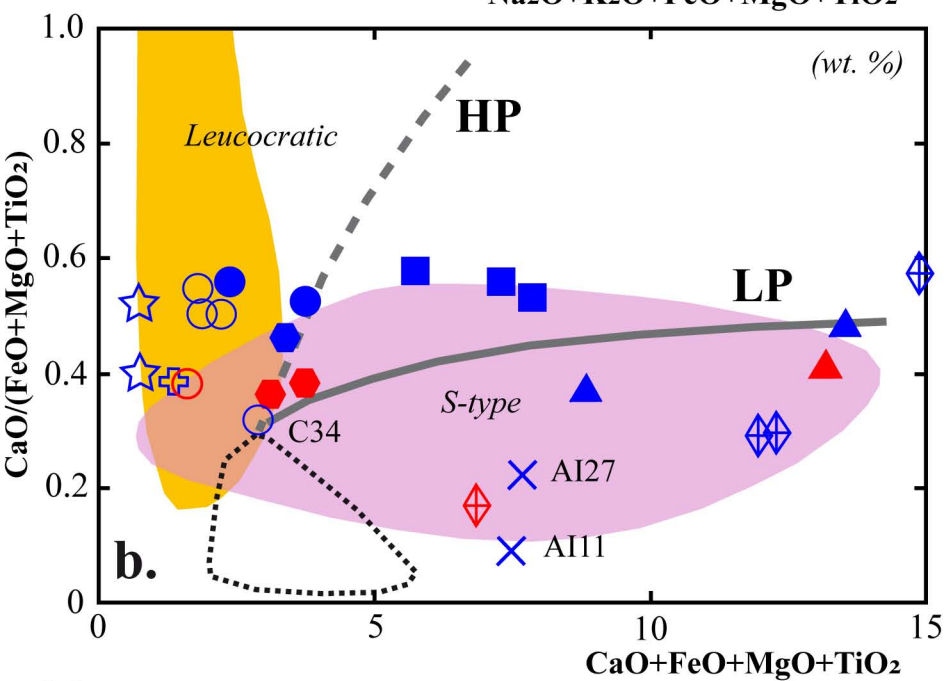
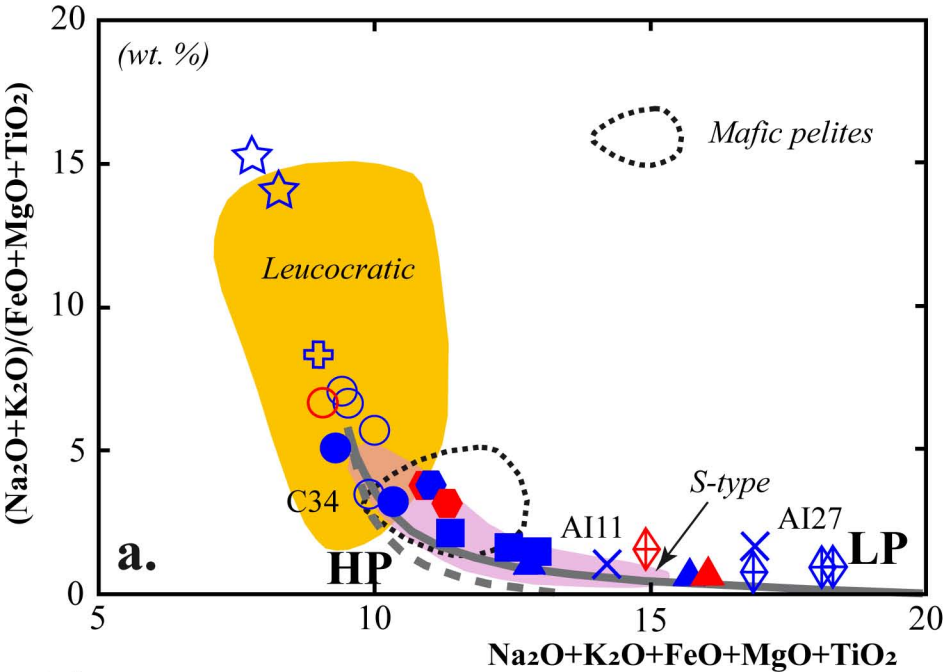


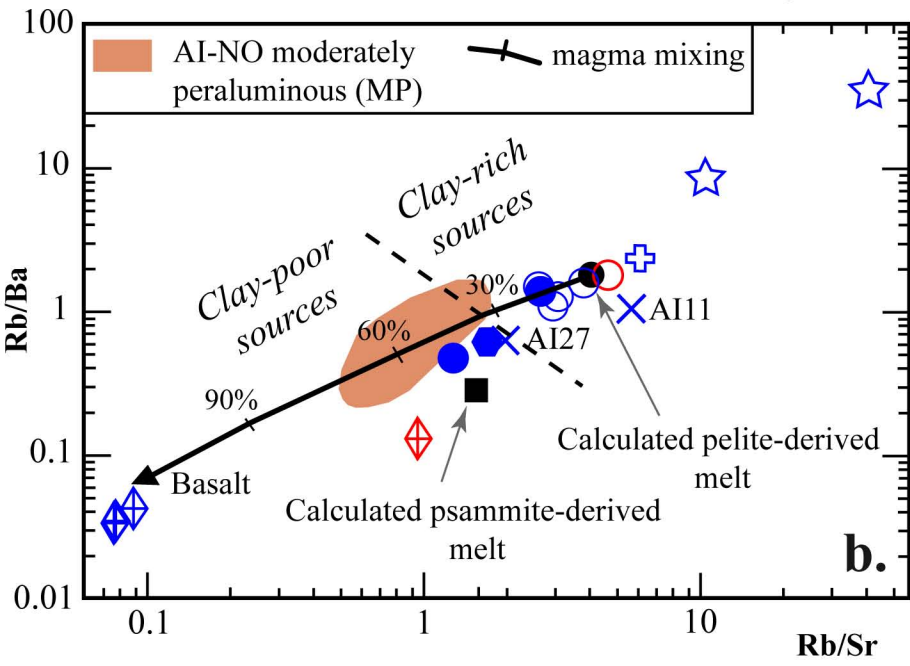
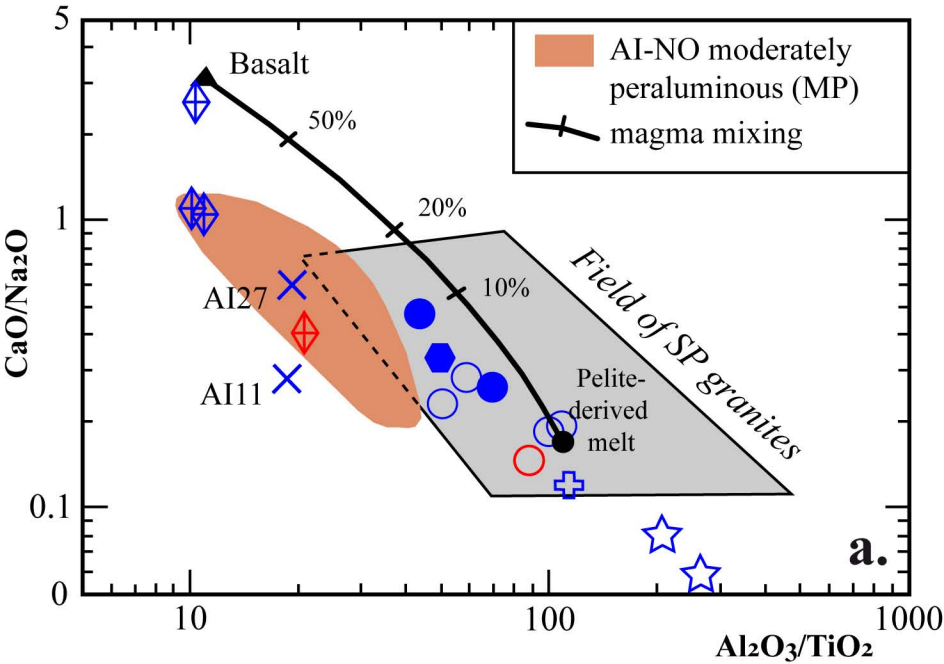


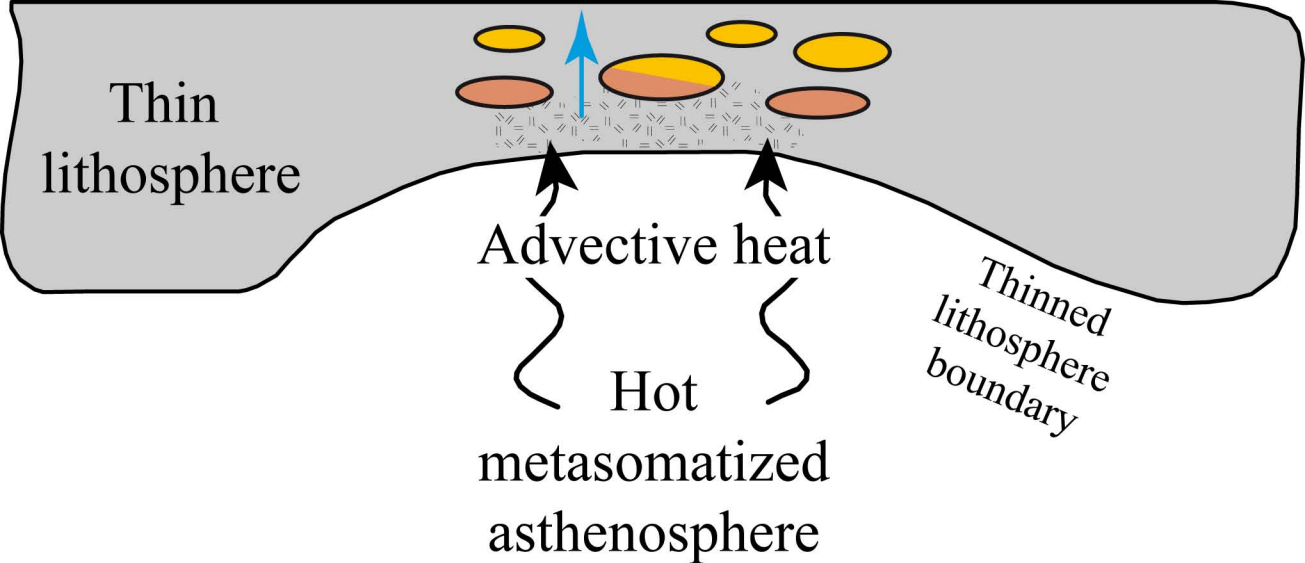












-  High-K alkali-calcic moderately peraluminous granitoid
-  Strongly peraluminous leucogranite
-  Mixing of mantle- and crustal-derived melts
-  Lamprophyre dyking